

ABSTRACT

EFREMENKO, ALINA YURIEVNA. Theoretical and Experimental Spectroscopic studies of Conducting Metal Oxide Thin Films. (Under the direction of Stefan Franzen.)

In order to expand on the growing field on Surface Plasmon Resonance Spectroscopy (SPRS) the application of SPRS to Conducting Metal Oxides (CMO) was studied. Through experimental and theoretical studies it was concluded that CMO's are capable of sustaining Surface Plasmon Polaritons (SPP) like those in noble metals. Specifically, we have used indium tin oxide (ITO) as a test case to demonstrate the interplay of experiment and theory. Theoretical studies provided an excellent basis for comparison to experimental data. Furthermore, Near Edge X-Ray Absorption Fine Structure Spectroscopy (NEXAFS) was applied in order to examine the ITO as a substrate for self assembled monolayers (SAMs). It was found that hexadecanethiol and phosphonic acid form ordered monolayers on ITO.

Theoretical and Experimental Spectroscopic studies of Conducting
Metal Oxide Thin Films

by
Alina Yurievna Efremenko

A thesis submitted to the Graduate Faculty of
North Carolina State University
In partial fulfillment of the
Requirements for the Degree of
Master of Science

Chemistry

Raleigh, North Carolina

2009

APPROVED BY:

Stefan Franzen
Chair of Advisory Committee

Jon-Paul Maria

Lin He

DEDICATION

I would like to dedicate this to Polina, my little cousin. It was her diagnosis of diabetes at the age of two that sparked my interest in science.

I love you Polisha!

BIOGRAPHY

I was born on Sunday September 19th, 1982 to Natalia and Yuri Efremenko in Moscow, Russia. I lived in Russia till the summer of 1992 when we moved to Oak Ridge, TN. I graduated from Farragut High School in Knoxville, TN. When Polina, my cousin, got sick I was at the hospital with her. The doctor said by the time she graduates high school they will have a pill instead of a shot for her diabetes. It was then that I thought what an amazing thing science is to be able to do that for someone. I went to the University of Tennessee, Knoxville or Big Orange Country where I received a Bachelor of Science. After studying in St. Etienne, France I moved to Raleigh, NC to attend graduate school at North Carolina State University.

I am an outgoing person who sees the good in everything and actually believes in world peace. I am a huge sports fan, a devoted pool player, a musician at heart, a world traveler, and a sometimes fearless skier. I love animals and people and would do anything for either. I believe in the simple things that make you happy such as hearing your favorite song on the radio when you get in the car or the twinkling of Christmas lights. My favorite thing in the world is to laugh and to make others laugh or at least smile. I like to leave big decisions for the morning and believe that everything happens for the best.

ACKNOWLEDGEMENTS

I would first like to acknowledge from my professional life Dr. Stefan Franzen for being my advisor and providing me with the tools to make my research possible here at NCSU. Dr. Crissy Rhodes for teaching me the ropes, believing in me, and all your work on this project, Rich Kelly for always having a hug and an ear for me, Dustin Lockney for your positive attitude, Mike Davis for the walks, Rob Schmidt for being my study partner, Johnny Gaff for being a realist, Matt Thompson for all the nice things you have said, and Dr. Marta Cerruti for all the interesting things you taught me. Also a special thanks to Dr. David Aspnes for all the physics you taught me, Dr. Jan Genzer for all the NEXAFS work, Dr. Jon-Paul Maria, Dr. Mark Losego for making these studies possible, and Dr. Lin He for your helpful comments.

On a personal note I would like to first and foremost thank my parents Natalia and Yuri, for always pushing me to do my best and all of the amazing opportunities you have given me over the years, you were always my first choice for parents. Thank you to my grandparents, Valya, Svetlana, Alesha, Svetlana, and everything they have done for me over the years and all their words of wisdom. Nadya for understanding me better than anyone else, Andrej for your helpful hints about graduate school, and Alesha and Denis for making me smile. Thank you Misha for teaching me so much when I was younger, Inna for always being so incredibly kind, and Boris and Polina for making me happy. To my

oldest friend in the world, I'm glad it's you; I wouldn't change that for anything, thank you Olga. Thank you to the Ovchinnikov family for always opening your house to me. Thank you Ella and Vika Kozyr for all the helpful incites you have given me and Sasha Kozyr for treating me like a daughter. Thank you to Leslie and Andy for always being there. Thank you Becca, I don't even know where to start!!! Katie Egan you are the best, thanks for always being honest. Thank you Chris Acuff you have always being so kind to me. Thank you Anastasia without you Raleigh would not have been the same. Rachel Bender thank you for being my partner in crime and a great dancer. I have many more people to thank since in their own way they have had an influence on me. I wish I could name them all but since the past couple of year's I've been living in Raleigh these come to mind: Katie Schatz, Jean Wan, Jerri Yates, Dave Arney, Richy Innis and Marianna Chriscoe. Thank you to everyone I know you have made an impact on my life and I am grateful.

TABLE OF CONTENTS

	Page
LIST OF TABLES	viii
LIST OF FIGURES	ix
Chapter 1 Introduction	1
1.1 An Introduction to Surface Plasmon Resonance	1
1.2 Surface Plasmon Resonance Spectroscopy Instrumentation	3
1.3 Surface Plasmons in Noble Metals	4
1.4 Indium Tin Oxide.....	5
1.5 Near Edge X-Ray Absorption Fine Structure Spectroscopy.....	5
1.6 Summary of the Introduction.....	6
Chapter 2 Theory Behind Surface Plasmon Resonance	7
2.1 Drude Free Electron Model	7
2.2 Fresnel Equations.....	8
2.3 Theoretical Calculations: Introduction	9
2.4 Two Layer Model: Prediction of the Dispersion Curve.....	11
2.5 Three Layer Model: Application to Experiment.....	13
2.6 Exploration of the Poles.....	15
2.6.1 Case 1: $n_{o\perp} \rightarrow 0$	16
2.6.2 Case 2: Real $n_{o\perp}$	18
2.6.3 Case 3: Imaginary $n_{o\perp}$	20
2.6.4 Case 4: All are Imaginary	22
2.7 Conclusion	22
Chapter 3 Materials and Methods.....	23
3.1 Surface Plasmon Resonance Data Collection.....	23
3.2 Overlayer Preparations.....	23
3.2.1 Carrier Concentration Series for ITO on BK7 glass.....	23
3.2.2 Mobility Series for ITO on BK7 glass.....	24
3.2.3 Overlayer Preparation on Silicon.....	24
3.3 Monolayer preparation.....	25
3.3.5 Hexadecanethiol.....	25
3.3.6 Octadecylphosphonic Acid	26
3.4 Near-edge x-ray absorption fine structure (NEXAFS) Spectroscopy.....	26
3.5 Atomic Force Microscopy	27
Chapter 4 Experimental and Theoretical Results and Comparison	28
4.1 Introduction.....	28
4.2 Effect of Film Thickness.....	28
4.3 Effect of Carrier Concentration	29
4.4 Effect of Electron Mobility.....	30
4.5 Experimental Data Compared to Theoretical Data.....	31
4.5.1 Thickness Series.....	31

4.5.2 Carrier Concentration.....	33
4.5.3 Mobility Series.....	35
4.5.4 Influence of Substrate Index of Refraction on SPP	37
4.6 Exploration of Different Substrates; Consideration of the Generality of	39
the SPR Effect for Conducting Metal Oxides.....	39
4.7 Conclusion	42
Chapter 5 Near Edge X-ray Absorption Fine Structure Spectroscopy of Self	
Assembled Monolayer on Indium Tin Oxide Thin	45
5.1 Introduction to NEXAFS	45
5.2 Normalization of the Data.....	46
5.3 Hexadecanethiol Orientation	46
5.4 Calculating Tilt Angles	49
5.5 Phosphonic Acid Tilt Angles	50
5.6 Conclusion	53
APPENDICES	56
Appendix A Evaluating the Denominator for s-polarized Light	57
Appendix B Supporting Data for NEXAFS Calculations	61

LIST OF TABLES

	Page
Table 1 <i>The calculated tilt angles for the pressure series with octadecylphosphonic acid are shown.</i>	53

LIST OF FIGURES

Page

CHAPTER 1

Figure 1 Calculated surface plasmon resonance (SPR) curves at 830-nm excitation for (solid line) a three-layer system composed of an SF-10 glass prism ($n = 1.711$), a 45.0-nm-thick Au film ($n_D 0.165 = 5.205i$), and an infinite layer of water ($n = 1.327$) and (dashed line) a four-layer system composed of an SF-10 glass prism ($n = 1.711$), a 45.0-nm-thick Au film ($n = 0.165 + 5.205i$), a 5.0-nm-thick biopolymer film ($n = 1.45$), and an infinite layer of water ($n = 1.327$)..... 2

Figure 2 a) The Kretschmann configuration and b) The Otto configuration. The prism is referred to as the ambient, the CMO as the overlayer, and air as the substrate. (Figure was taken from a public domain) 4

CHAPTER 2

Figure 3. A) The Kretschman Configuration with the excitation of an evanescent wave. B) The x- component excited along the surface with an angle of incidence theta, θ . (Figure taken from Reference 4)..... 10

Figure 4. Dispersion curve for a two-phase model of ITO using only the real part of the dielectric response. (Figure taken from Reference 4)..... 12

CHAPTER 4

Figure 5 The graph of $\ln(\text{pressure of oxygen gas})$ during the post annealing process versus the carrier concentration determined by Hall Effect Measurement. Each of the original pressures is listed next to the appropriate data point..... 30

Figure 6 The graph of seven substrates with target gas pressure of 7mTorr, 8.5mTorr, 9mTorr, 10mTorr, 12mTorr, 15mTorr, and 20mTorr versus the measure mobility of each..... 31

Figure 7 Experimental data (A-D) collected showing varying thickness of ITO on BK7 glass, theoretical calculation for the series (E-H)..... 32

Figure 8 Experimental data (M-O) collected showing varying thickness of ITO on BK7 glass, theoretical calculation for the series (P-R)..... 33

Figure 9 The experimental and theoretical data for the carrier concentration series. The partial pressure of oxygen for A and E is 0.01 mTorr, B and F 10^{-4} mTorr, C and G 10^{-5} mTorr, and D and H 10^{-7} mTorr..... 35

Figure 10 Varied pressure of the targeting gas changes the mobility cause a greater peak width. Where the sputtering pressure of the target gas is 6 mTorr for A and E, 9 mTorr for B and F, 12 mTorr for C and G, and 15 mTorr for D and H..... 37

Figure 11 Comparison of substrates, BK7(left) vs SF10 (right) glass.	38
Figure 12. Comparison of substrates, BK7 vs SF10 glass.....	39
Figure 13 Theoretical Calculations for AZO, SFO, and CTO compared to ITO...	41
Figure 14 Dispersion curves for ITO, AZO, and CTO.	42

CHAPTER 5

Figure 15 The pressure series of ITO on Silicon. The AFM data on the right corresponds in location to the NEXAFS data on the left. The differences plots are located in their corresponding graphs. A) 6 mTorr RMS 0.91 nm B) 7 mTorr RMS 0.78 nm C) 8.5 mTorr RMS 1.7 nm D) 10 mTorr RMS 2.0 E) 12 mTorr 1.1 nm and F) 20 mTorr 6.6 nm. The green lines are the grazing at 20°, black is the normal at 90°, and blue is the magic at 55°.	48
Figure 16 The annealing series of ITO on Silicon. The AFM data on the right corresponds in location to the NEXAFS data on the left. The differences plots are located in their corresponding graphs. A) Amorphous RMS 0.28 nm B) 100°C RMS 0.34 nm C) 200°C RMS 0.63 nm D) 300°C RMS 0.75 nm E) 400°C 1.2 nm and F) 500°C 1.0 nm. The green lines are the grazing at 20°, black is the normal at 90°, and blue is the magic at 55°.	49
Figure 17 Example of fitted data. The blue line underneath the red is the normalized experimental data while the red is the summation of the adjusted intensities identified by the difference spectra shown in yellow. The graphs shown are for sample out of the pressure series, 6 mTorr. The graph on the left is at 20° and on the right is 90°.	51
Figure 18 The top graph shows the peak area for the 1s →σ _{C-H} * and the bottom graph show the peak are for the 1s →σ _{C-C} *. Each of the lines represents different chain tilt angles (starting at 10°, shown on graph, 20, 25, 30, 35, 40, 45, 50, 55, shown on graph) evaluated using Reference 7.....	52

Chapter 1 Introduction

1.1 An Introduction to Surface Plasmon Resonance

The study of Surface Plasmon Resonance (SPR) has emerged as an established field in the last few decades. The existence of surface plasmons in metal thin films is the basis for SPR technology. Surface Plasmons are oscillating modes of free electron density existing in a metal thin film. (1) The plasmon phenomenon arises from the intrinsic ability of the conducting electrons to oscillate in a collective manner. The excitation of a plasmon with electromagnetic radiation is known as a Surface Plasmon Polariton (SPP). SPP cannot be excited with light at the metal/substrate, for example gold/air or gold/water, interface because coupling conditions cannot be satisfied therefore a prism configuration is used for wavevector matching. During total internal reflection an evanescent wave propagates from the prism/metal interface along the z-axis to the metal/substrate interface exciting the SPP. The damping which results due to this excitation leads to absorption. When the appropriate condition is met for coupling of light into the conductor to drive a SPP, a sharp drop in reflectance is observed. Since the reflectance of the SPP is found to be highly angle dependent, the angle of incidence determines the wavenumber where the reflectance drop is found. The location of the SPP is therefore influenced by the indices of refraction, n , of the metal and the substrate, by $k = n\omega/c$ where k is part of the wave. Changing the

index of refraction with the addition of a film, such as a biopolymer will change the angle of incidence and therefore changing the angle and frequency dependence of the SPP. Figure 1 shows a bare 45 nm gold thin film deposited on SF-10 glass and an infinite layer of water, solid line, and a 45 nm gold film thin film with a 5.0nm thick biopolymer film with an infinite layer of water, dashed line. The addition of the bio-molecules results in an angle shift. SPR is convenient for bio-sensing studies due to its sensitive reaction to changes in the index of refraction.

SPR's sensitivity to optical properties has allowed for other uses such as real-time interactions at the interface using flow cells without the use of labeled molecules, characterization of thin films, and gas detection. (2) SPR technology is also convenient since thin films are not destroyed during measurement.

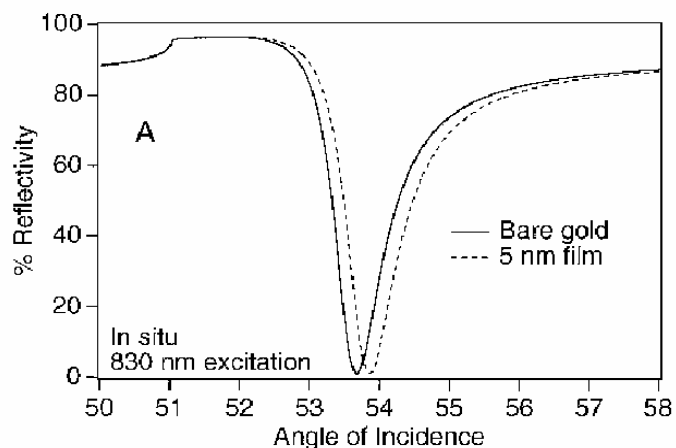


Figure 1 Calculated surface plasmon resonance (SPR) curves at 830-nm excitation for (solid line) a three-layer system composed of an SF-10 glass prism ($n = 1.711$), a 45.0-nm-thick Au film ($n D 0.165 = 5.205i$), and an infinite layer of

water ($n = 1.327$) and (dashed line) a four-layer system composed of an SF-10 glass prism ($n = 1.711$), a 45.0-nm-thick Au film ($n = 0.165 + j5.205i$), a 5.0-nm-thick biopolymer film ($n = 1.45$), and an infinite layer of water ($n = 1.327$)

(Figure one and caption is taken from reference one)

1.2 Surface Plasmon Resonance Spectroscopy Instrumentation

Boundary conditions must be met in order to achieve SPP excitation. Two common configurations for surface plasmon spectroscopy have been presented by Otto and by Kretschmann. (3) These geometries use a prism in order to refract the light toward the surface of the metal thin film and total internal reflection where after the critical angle is reached light can pass into the second medium. The Otto configuration leaves a small space between the prism and the metal achieving the excitation of the SPP with an evanescent wave. The Kretschmann configuration sets the prism directly on top of the ambient, a surface with the same index of refraction as the prism, on the opposite side of the metal thin film. The later is a more common configuration since it allows the substrate to be changed. Furthermore, the Otto configuration requires the space between the ambient and the metal to be exact over the entire area of the measurement. Both configurations can be seen in Figure 2. (3)

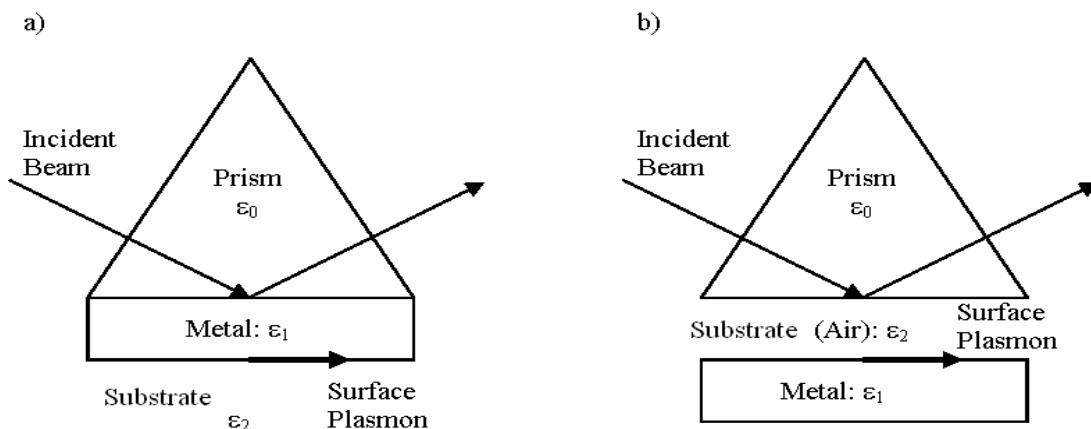


Figure 2 a) The Kretschmann configuration and b) The Otto configuration. The prism is referred to as the ambient, the CMO as the overlayer, and air as the substrate. (Figure was taken from a public domain)

1.3 Surface Plasmons in Noble Metals

Most studies of SPR have focused on noble metals such as gold and silver. The SPP of these thin films occurs in the visible electromagnetic spectrum below $20,000 \text{ cm}^{-1}$, and $30,000 \text{ cm}^{-1}$, respectively, making them convenient for bio-sensing. The d-band energies lower as the occupancy of d-electrons increases. The d-band in silver and gold is lower than the conduction band permitting band-to-band transitions that can mix with the plasmon oscillations. This situation permits the plasmons of gold and silver to derive oscillator strength from the d-sp transition. Because of this, the plasma frequencies of gold and silver are in the visible and the near-ultraviolet (UV), respectively. Without such an admixture of band-to-band transitions into the conduction band, other metals exhibit plasma frequencies in the far-UV. However, a conducting metal oxide,

CMO, such as indium tin oxide, ITO, does not exhibit interband transition but shows a plasmon in the near-infrared (IR). The existence of this plasmon is therefore believed to be due to free-carrier electrons existing in ITO. It is therefore our focus has been on investigating this phenomenon on conducting metal oxides (CMO). (4)

1.4 Indium Tin Oxide

One of the reasons ITO was chosen for SPR development is the convenient location of SPP in the near-IR 6000 cm^{-1} . ITO is already used as an infrared reflector and transparent electrode in the visible region of the electromagnetic spectrum. This permits ITO to be used in optical and electronic applications such as heat shielding and as a Faraday cage in computer monitors. Furthermore, ITO has variable parameters such as carrier concentration and mobility, which allows understanding what effect these properties have on SPR. [5].

1.5 Near Edge X-Ray Absorption Fine Structure Spectroscopy

In order to further expand on biosensor development Near Edge X-ray Absorption Fine Structure Spectroscopy (NEXAFS) measurement were performed on Self Assembled Monolayers (SAMs) on ITO. NEXAFS experiments conducted using the synchrotron light source at Brookhaven National Laboratory. NEXAFS measurements permit the determination of the orientation of the SAMs on the surface of the substrate. The motivation behind these experiments is to

determine which SAM's can be used in bio-molecule attachments on ITO. Once this has been done SPR spectroscopy can be used to measure the SPP response to the attachment of a bio-molecule. Currently the SAMs with the best order parameters have been created using hexadecanethiol and octadecylphosphonic acid.

1.6 Summary of the Introduction

The Surface Plasmon Resonance field has been growing exponentially in the past decades. One goal of the present work is the expansion of the substrates used in SPR bio-sensor technology to include CTO, specifically ITO in the greater part of this thesis. This particular substrate was a good starting point for experimental studies due to the tunability of its conductivity and electron mobility. Furthermore the application of NEXAFS spectroscopy permitted the determination of the organization of SAM's on ITO. Hopefully, the publication of these findings will encourage the exploration of other CTO as substrates for SPR bio-sensors.

Chapter 2 Theory Behind Surface Plasmon Resonance

2.1 Drude Free Electron Model

The theoretical principles that govern surface plasmons are described by the Drude model and Fresnel equations. The Drude model is an approximate description of the transport properties of electrons in materials. Drude assumed the simplest model for behavior of electrons in a metal. In this model the metal behaves like an empty box and each atom contributes its outer conduction electron, for example a monovalent atom contributes one electron. The electrons exist in an independent cloud with no interaction with the metal surface. After a collision occurs the electrons change magnitude and direction with no influence from previous velocities. Between collisions all other interactions are ignored. The time between collisions is referred to as the relaxation time, which is independent of the velocity or direction of electrons. Finally, there is scattering, that is, interaction with the lattice ions, which results in resistance. If a constant external field is applied the electrons are accelerated for a time but then undergo a collision that as noted above is assumed to randomize their direction. Upon averaging over an extended period of time the motion averages out to a constant drift velocity in the direction of the applied field. These assumptions allowed Drude to develop the equation of the motion for the drift velocity of charge carriers, or electrons. In microscopic terms the motion is a damping constant:

$$m \frac{d^2 x}{dt^2} = -\Gamma \frac{dx}{dt} + eE(t) \quad (1)$$

With suitable averaging this equation can be used to relate the mobility, the relaxation time, and the carrier concentration to the fundamental parameters describing motion on the atomic scale. These can then be used to evaluate the complex dielectric function of the material. The dielectric function in turn leads to the Drude Plasma frequency. In an actual physical metal the Drude model describes the behavior of the charge carriers inside the metal in terms of mobility and damping, but there are still interactions at the interface to consider.

2.2 Fresnel Equations

The Fresnel equations for two phases describe the behavior of light as it moves from one semi-infinite medium to the next. Both reflection and refraction occur as light passes from a first medium to a second one of different index of refraction. The Fresnel equations, shown later in the text, are used to calculate the reflection and transmission coefficients for light entering the surface. The three-phase model combines the effects at the ambient/metal and metal/substrate interface with propagation in the film to show the overall effect. The theoretical calculations below for the SPR phenomenon were carried out using the Drude model of the dielectric function and the Fresnel equations to determine the reflectance of two- and three-phase geometries.

2.3 Theoretical Calculations: Introduction

Theoretical calculations were performed to compare model predictions to the data. The calculations conducted done using the three phase model and the MATLAB code that can be found in the appendix. The three phases used in these calculations are air, a, conducting metal oxide, o, and substrate, s. In practice for the substrate we used BK7 or SF10 glass. The refractive indices for glass and air are 1.52 and 1.0, respectively. However, the optical behavior of conducting metal oxide films on a substrate is more complex. To find the optical behavior we used the Drude free electron model beginning with a calculation of the plasma frequency. This is done with (equation formatting in the text needs to be redone using that which I used above for Eq. (1)) using equation 2:

$$\omega_p = \sqrt{\frac{e^2 n}{m_e \epsilon_0}}, \quad (2)$$

where e is the electron charge, n is the carrier concentration, m_e is the effective mass, and ϵ_0 is the permittivity of free space.

The excitation occurs due to p-polarized light or the parallel component. In the coordinate system used here the electric vector of the s-polarized light, the perpendicular, is along the y-axis and the electric vector of the p-polarized light has projections along the x- and z-axes (Figure 3). The p-polarized wave decays exponentially in the z direction, hence this wave is evanescent. The characteristic lengths of decay above and below the surface are given by solving

the dispersion equation. The x component of the wave vector is excited along the surface.

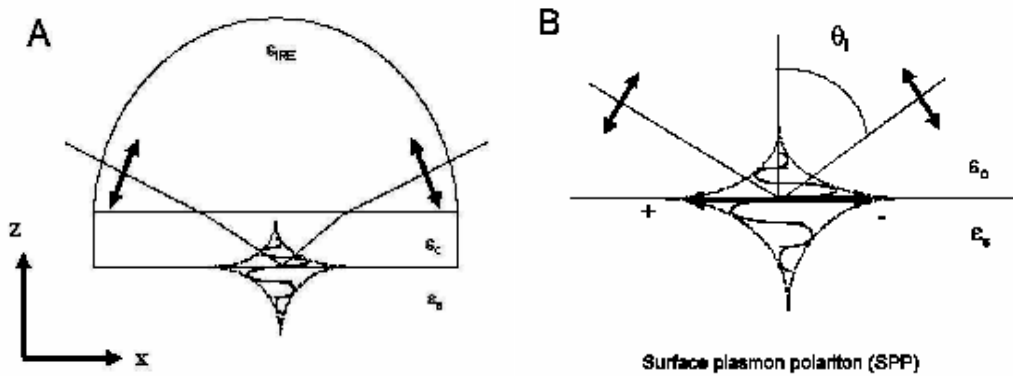


Figure 3. A) The Kretschman Configuration with the excitation of an evanescent wave. B) The x- component excited along the surface with an angle of incidence theta, θ . (Figure taken from Reference 4)

While both s- and p-polarized light contribute to reflectance, only the denominators of p-polarized waves can vanish, leading to plasmons. These excitations result in dips in the reflectance spectra as a function of the wavenumber of light. For s-polarized light similar dips may be seen, but these occur as a result of the numerator becoming small and are not the effects of collective excitations. They lead to the anti-resonance phenomenon that is seen at higher wavenumbers in our data. We present reflectance data as the ratio of p- to s-polarized reflectance, R_p/R_s .

The dielectric function is related to the complex refractive index squared.

By solving the Drude model we find

$$\varepsilon(\omega) = \varepsilon_{\infty} - \omega_p^2 \frac{1}{\omega^2 + i\omega\Gamma} \quad (3)$$

Where ε_{∞} is the infrared dielectric constant for the metal oxide, and has the values 3.8, 3.24, and 6.76 for ITO, AZO, and CTO, respectively. The angular frequency ω is proportional to the wavenumber, and Γ is the damping constant that as discussed above can be calculated using $\Gamma = e / (\mu m_e)$ or $1/\tau$, where μ is the electron mobility, m_e is the effective mass of the conducting metal oxide (ITO~0.4, CTO~0.4, AZO~.28) and τ is the relaxation time.

2.4 Two Layer Model: Prediction of the Dispersion Curve

A previous treatment of the two-phase model for ITO by Franzen predicted the appearance of the Surface Plasmon Polariton (SPP) and the radiative plasmon polariton (RPP) using the dispersion curve shown in Fig. 4. (4) The dispersion curve involves only the real part or the in-phase contribution of the dielectric function. For the SPP to be driven, the wave vector of the incident light and the wave vector of the SPP must be matched at the interface. The screened plasma absorption, ω_{sp} , represents the maximum possible frequency of light for which coupling can occur. A light line, angle of 70° , is shown to intersect the SPP dispersion curve. Coupling of electromagnetic radiation occurs at this

intersection. Experimentally this is done with the use of the Kretschmann configuration, where a prism with an index of refraction greater than that of the film is used to ensure wave vector matching as shown in Fig. 2A. The calculation for the dispersion curve, Figure 4, is done by using the real part of equation 3, $\epsilon_{\text{real}} = \epsilon_{\infty} - \omega_p^2 / (\omega^2 + \Gamma^2)$, and the response along the interface, which can be seen in Figure 3, $n_x = k_x c / \omega = (\epsilon_s \epsilon_c / (\epsilon_c + \epsilon_s))^{1/2}$. We used 900 cm^{-1} for the damping constant and $\omega_p = 17,700 \text{ cm}^{-1}$, which was obtained from a data fit of the free electron model to ITO. The quantity ω/c is the frequency range from 0 to $12,000 \text{ cm}^{-1}$, and is plotted on the y-axis versus the wave vector, k_x , shown on the x-axis.

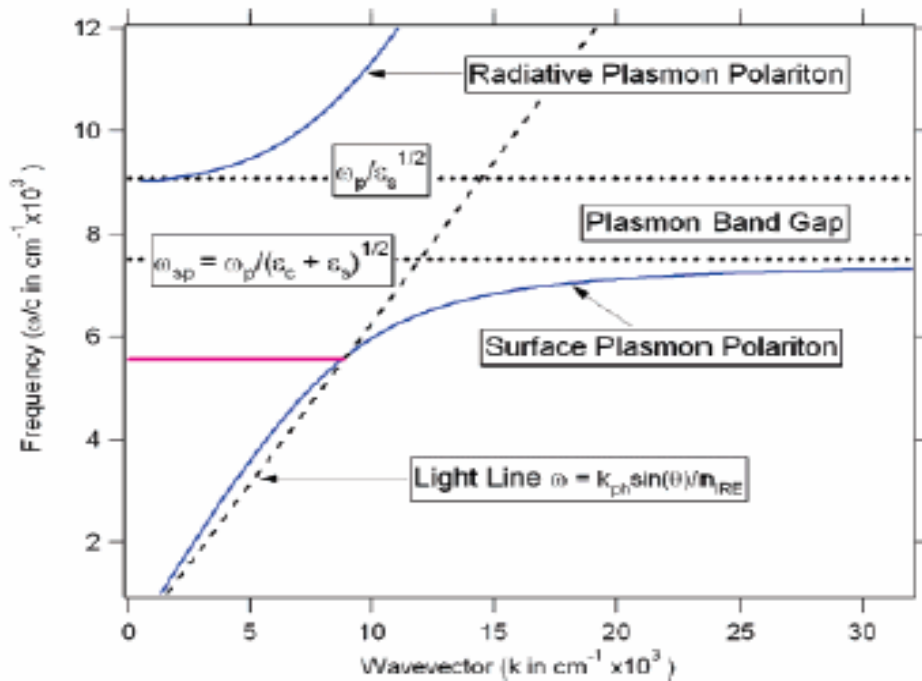


Figure 4. Dispersion curve for a two-phase model of ITO using only the real part of the dielectric response. (Figure taken from Reference 4)

2.5 Three Layer Model: Application to Experiment

The theoretical models allows for the calculation of the theoretical optical parameters which can then be compared to the experimental data. The angle θ used in these calculations is the angle between the surface normal and that of light propagation in the prism, Figure 3b. We cover the range from the critical angle to grazing incidence. The dielectric response for each layer includes the intrinsic dielectric response of the material, the index of refraction of the first layer and θ . The equations can be found below, equations 4-6, and are rewritten for the in terms of the complex dielectric in equations 7-9:

$$\mathcal{E}_s = n_{s\perp}^2 + n_x^2 \quad \mathcal{E}_a = n_{a\perp}^2 + n_x^2 \quad \mathcal{E}_o = n_{o\perp}^2 + n_x^2 \quad (4-6)$$

$$n_{o\perp} = \sqrt{\mathcal{E}_o - \mathcal{E}_s \sin^2 \theta} \quad n_{a\perp} = \sqrt{\mathcal{E}_a - \mathcal{E}_s \sin^2 \theta} \quad n_{s\perp} = \sqrt{\mathcal{E}_s - \mathcal{E}_s \sin^2 \theta} \quad (7-9)$$

The Fresnel equations for light at interfaces between materials of different indices of refraction are applied to calculate the contributing components of s- and p-polarized light at each boundary. We find

$$r_{s,oa} = \frac{n_{a\perp} - n_{o\perp}}{n_{a\perp} + n_{o\perp}} \quad r_{s,so} = \frac{n_{o\perp} - n_{s\perp}}{n_{o\perp} + n_{s\perp}} \quad (10-11)$$

$$r_{p,oa} = \frac{\mathcal{E}_o n_{a\perp} - \mathcal{E}_a n_{o\perp}}{\mathcal{E}_o n_{a\perp} + \mathcal{E}_a n_{o\perp}} \quad r_{p,so} = \frac{\mathcal{E}_s n_{o\perp} - \mathcal{E}_o n_{s\perp}}{\mathcal{E}_s n_{o\perp} + \mathcal{E}_o n_{s\perp}} \quad (12-13)$$

where $r_{s,oa}$, $r_{s,so}$, $r_{p,oa}$, and $r_{p,so}$ are the reflection coefficients for the interfaces between ambient/overlayer and overlayer/substrate. These terms are combined for each of the s- and p-polarized components, equations 14-15 and 16. The numerators of the equations represent interference involving back-reflected waves at the o-a and s-o boundaries, while the denominator represents the relative effect of back-reflected component. The component β represents the light reflected back due to the ITO phase to the detector. Since the substrate is the third phase, no reflection is observed below it. This is the boundary condition for the problem. The equations are therefore

$$r_{s,soa} = \frac{r_{s,oa} + r_{s,so} e^{2i\beta}}{1 + r_{s,oa} r_{s,so} e^{2i\beta}} \quad r_{p,soa} = \frac{r_{p,oa} + r_{p,so} e^{2i\beta}}{1 + r_{p,oa} r_{p,so} e^{2i\beta}} \quad (14-15)$$

$$\beta = 2 \pi n_o \left(\frac{d}{\lambda} \right) \quad (16)$$

Equation (16) is used to calculate β where d is the thickness of the ITO layer and λ is the wavelength. The r_s and the r_p components are then squared since the r_s is a spiral component and its square, the power reflectance, R_s , exhibits interference. The ratio of r_p/r_s light gives the spectrum that is shown in the model calculation, equation 17.

$$Spectrum = \frac{|r_p^2|}{|r_s^2|} \quad (17)$$

Theoretical calculations using the method above were performed for three different experimental series, 1.) the thickness series, 2.) carrier concentration series, and 3.) mobility series. Furthermore the code was also used in helping to understand the effect on the SPP if the index of refraction of the glass was changed as well as changing the CMO itself. These calculations will be discussed below.

2.6 Exploration of the Poles

The Fresnel equations can be used to find conditions for which the plasmon can be driven. Since the plasmon is self sustaining, in principle it does not need an incident wave to initiate it or to keep it going, although with absorption an plasmon once excited dies out after a finite amount of time unless it is sustained by an incident wave. Therefore, to find plasmons we need only look for solutions that have only outgoing waves for no incoming waves. The combined three-phase Fresnel equation, equations 14 and 15, represent the outgoing and incoming waves through the numerator and denominator respectively. By finding the solutions where the denominator vanishes and verifying that the numerator does not vanish under these conditions we identify the conditions for the existence of a plasmon.

To find the solution the denominator is first set to zero. The equations for the two-phase r_{oa} and r_{so} , equations 12 and 13, are inserted in the equation for $r_{p,soa}$, equation 14, and the denominator is then set to zero:

$$0 = 1 + r_{s,oa} r_{s,so} e^{2i\beta} = 1 + \left(\frac{\epsilon_o n_{a\perp} - \epsilon_a n_{o\perp}}{\epsilon_o n_{a\perp} + \epsilon_a n_{o\perp}} \right) \left(\frac{\epsilon_s n_{o\perp} - \epsilon_o n_{s\perp}}{\epsilon_s n_{o\perp} + \epsilon_o n_{s\perp}} \right) e^{2ik_{o\perp}d} \quad (18)$$

where:

$$\beta = 2\pi n_o \left(\frac{d}{\lambda} \right) = 2\pi n_o d \left(\frac{f}{c} \right) = 2\pi n_o d \left(\frac{\omega}{2\pi c} \right) = 2\pi n_o d \left(\frac{ck_{o\perp}}{2\pi cn_{o\perp}} \right) = k_{o\perp} d \quad (19)$$

Equation 18 is expanded and the real and imaginary parts are grouped together resulting in:

$$0 = \epsilon_o n_{o\perp} (\epsilon_s n_{a\perp} + \epsilon_a n_{s\perp}) \cos(k_{o\perp} d) - i (\epsilon_a \epsilon_s n_{o\perp}^2 + \epsilon_o^2 n_{a\perp} n_{s\perp}) \sin(k_{o\perp} d) \quad (20)$$

Now the different possibilities for $n_{o\perp}$, $n_{a\perp}$, $n_{s\perp}$, and d can be explored to find the plasmon solution.

2.6.1 Case 1: $n_{o\perp} \rightarrow 0$

The first case explored is the limit of $n_{o\perp}$ approaching zero. If $n_{o\perp} = 0$ is inserted into equations for r_{oa} , r_{so} , and β the result is $r_{oa} = 1$, $r_{so} = -1$, and $e^{2ik_{o\perp}d} = 1$, therefore both numerator and denominator are zero and it is impossible to determine whether there is a pole. An expansion is needed and each of the separate two-phase equations approximates to:

$$r_{p,oa} \cong 1 - 2 \frac{\epsilon_a n_{o\perp}}{\epsilon_o n_{a\perp}} \quad r_{p,so} \cong - \left(1 - 2 \frac{\epsilon_s n_{o\perp}}{\epsilon_o n_{s\perp}} \right) \quad e^{2ik_{o\perp}d} \cong 1 + 2ik_{o\perp}d \quad (21-23)$$

These approximations can be inserted into the original three-phase equation 15.

The resulting equation is expanded and $n_{o\perp}$ is set equal to zero to obtain:

$$r_{soa} \cong \frac{-\frac{\epsilon_a}{\epsilon_o n_{a\perp}} + \frac{\epsilon_s}{\epsilon_o n_{s\perp}} - i\frac{\omega}{c}d}{\frac{\epsilon_a}{\epsilon_o n_{a\perp}} + \frac{\epsilon_s}{\epsilon_o n_{s\perp}} - i\frac{\omega}{c}d} \quad (24)$$

Equation 24 can now be explored further by looking at the denominator and setting d equal to zero and using the dispersion relations, equations 4-6. The

result is $0 = \frac{\epsilon_a}{n_{a\perp}} + \frac{\epsilon_s}{n_{s\perp}}$ (25) or $\epsilon_a^2 n_{s\perp}^2 = \epsilon_s^2 n_{a\perp}^2$ (26) then with the dispersion

relations $\epsilon_a^2 (\epsilon_s - n_x^2) = \epsilon_s^2 (\epsilon_a - n_x^2)$ (27) finally this can be expanded and the like terms can be combined:

$$\epsilon_a \epsilon_s (\epsilon_a - \epsilon_s) = (\epsilon_a + \epsilon_s) (\epsilon_a - \epsilon_s) n_x^2 \quad \frac{\epsilon_a \epsilon_s}{(\epsilon_a + \epsilon_s)} = n_x^2 \quad (28-29)$$

The obvious solution for equation 25 is $\epsilon_a = \epsilon_s$ however this does not satisfy equation 25 unless the sign of $n_{a\perp}$ or $n_{s\perp}$ changed which is not allowed since both of these quantities must be positive. Therefore no solution is found with $n_{o\perp} \rightarrow 0$.

2.6.2 Case 2: Real $n_{o\perp}$

Case 2.1: $n_{o\perp}$, $n_{a\perp}$ and $n_{s\perp}$ are real

Returning to equation 20 and assuming that $n_{o\perp}$, $n_{a\perp}$ and $n_{s\perp}$ are real.

When this leaky-leaky waveguide is explored a solution is not possible since all of the $n_{x\perp}$ terms are real. The only other possibility is through simultaneous elimination of the cos and sin terms. Because this is not possible, there is no solution

Case 2.2: Either $n_{a\perp}$ or $n_{s\perp}$ is imaginary

Assuming now that the $n_{a\perp}$ term is imaginary, $n_{a\perp} \rightarrow in'_{a\perp}$, equation 20 is

now:

$$0 = \varepsilon_o n_{o\perp} (i\varepsilon_s n'_{a\perp} + \varepsilon_a n_{s\perp}) \cos(k_{o\perp} d) + (-i\varepsilon_a \varepsilon_s n_{o\perp}^2 + \varepsilon_o^2 n'_{a\perp} n_{s\perp}) \sin(k_{o\perp} d) \quad (30)$$

Further, the equation is expanded to bring together the real and imaginary terms:

$$0 = i\varepsilon_s n_{o\perp} (\varepsilon_o n'_{a\perp} \cos(k_{o\perp} d) - \varepsilon_a n_{o\perp} \sin(k_{o\perp} d)) + \varepsilon_o n_{s\perp} (\varepsilon_a n_{o\perp} \cos(k_{o\perp} d) + \varepsilon_o n'_{a\perp} \sin(k_{o\perp} d)) \quad (31)$$

Equation 31 can now be solved for the real and imaginary terms separately. The

simultaneous solution here leads to $0 = \frac{\varepsilon_o n'_{a\perp}}{\sin(k_{o\perp} d)}$ where the assumption is $\varepsilon_o > n_x^2$

and therefore cannot be solved with the allowed parameters.

Furthermore the possibility that $n'_{a\perp} \rightarrow 0$, a leaky waveguide, then the only

affected term is $r_{p,oa}$ and the assumption that $n_{a\perp}^2$ is canceled. The corrected term can be combined with $r_{p,soa}$ and the denominator is set to zero once again. However since no singularities exist for this solution and therefore $n_{a\perp} \rightarrow 0$ does not lead to a plasmon. The same logic can be applied to $n_{s\perp} \rightarrow in'_{s\perp}$ and no solution exists for this case either.

$$r_{p,oa} \cong -1 + 2 \frac{\epsilon_a n'_{a\perp}}{\epsilon_o n_{a\perp}} \quad r_{p,soa} = \frac{\left(-1 + 2 \frac{\epsilon_a n'_{a\perp}}{\epsilon_o n_{a\perp}}\right) + r_{s,so} e^{2i\beta}}{1 + \left(-1 + 2 \frac{\epsilon_a n'_{a\perp}}{\epsilon_o n_{a\perp}}\right) r_{s,so} e^{2i\beta}} \rightarrow 1 \quad (32)$$

Case 2.3 $n_{a\perp}$ and $n_{s\perp}$ are imaginary

Finally there is a possibility that both $n_{s\perp} \rightarrow in'_{s\perp}$ and $n_{a\perp} \rightarrow in'_{a\perp}$ which expands equation 20 to:

$$0 = i\epsilon_o n_{o\perp} (\epsilon_s n'_{a\perp} + \epsilon_a n'_{s\perp}) \cos(k_{o\perp} d) - i(\epsilon_a \epsilon_s n_{o\perp}^2 - \epsilon_o^2 n'_{a\perp} n'_{s\perp}) \sin(k_{o\perp} d) \quad (33)$$

Here a number of waveguides work as a solution, for example $\sin(k_{o\perp} d) = 0$ where the solution to the left side of the equation is if the inside of the parenthesis is equal to zero, which can be expanded like equations 28 and 29. This leads to the standard plasmon, equation 29, where the $\epsilon_a = \epsilon_s$ are ignored due to the lack of boundary, the ambient is air. The solution to the standard plasmon here is the waveguide having a thickness of zero.

2.6.3 Case 3: Imaginary $n_{o\perp}$

Case 3.1: $n_{a\perp}$ and $n_{s\perp}$ are real

The other possibility is that $n_{o\perp} \rightarrow in'_{o\perp}$ which sets equation 20 to:

$$0 = i\varepsilon_o n'_{o\perp} (\varepsilon_s n_{a\perp} + \varepsilon_a n_{s\perp}) \cos(hk'_{o\perp} d) - (\varepsilon_o^2 n_{a\perp} n_{s\perp} - \varepsilon_a \varepsilon_s n'^2_{o\perp}) \sin(hk'_{o\perp} d) \quad (34)$$

Here the solution can be explored by setting $k'_{o\perp} d \rightarrow 0$ and $\varepsilon_o \rightarrow 0$. This was done previously by exploring r_p and exploring the field internal to the film where d is limited with n_x going to 0. This solution corresponds to any external dielectric functions with an internal field perpendicular to the boundaries. With $\varepsilon_o = 0$ the left hand side of the equation can be eliminated and the solution is an electrostatic solution where n_x is small:

$$0 = -\varepsilon_a \varepsilon_s n'^2_{o\perp} \sin(hk'_{o\perp} d) \quad (35)$$

If both of the other n_x terms are real the only way to eliminate the cos term is with $\varepsilon_o = 0$ which is done above.

Case 3.2 $n_{a\perp}$ is real and $n_{s\perp}$ is imaginary

Furthermore if n_a is real and $n_{s\perp} \rightarrow in'_{s\perp}$ which is again used in equation 20. This can be expanded to an equation similar to equation 31 and once again the simultaneous solution:

$$0 = \frac{\varepsilon_s n_{o\perp}}{\sin(hk_{o\perp} d)} \quad (36)$$

One solution here is if $\varepsilon_s \rightarrow 0$ therefore the only term from equations 21-23 that

needs to be adjusted is the r_{so} which becomes $r_{p,so} \cong -\left(1 + 2\frac{i\varepsilon_s n_{o\perp}}{\varepsilon_o n_{s\perp}}\right) \cong -1$

therefore the equation for the three-phase Fresnel becomes: $r_{soa} \cong \frac{r_{oa} - e^{-2k'_{o\perp}d}}{1 - r_{oa}e^{-2k'_{o\perp}d}}$

and since r_{oa} is less than one, no poles are found.

The other possible solution is thickness going to infinity. The r_{oa} term will still not go to zero assuming that both $\varepsilon_o n_{a\perp}$ and $\varepsilon_o n'_{o\perp}$ so once again the r_{so} term is explored:

$$r_{p,so} = \frac{i\varepsilon_s n'_{o\perp} - i\varepsilon_o n'_{s\perp}}{i\varepsilon_s n'_{o\perp} + i\varepsilon_o n'_{s\perp}} \quad (37)$$

Once again this leads to $i\varepsilon_s n'_{o\perp} = -i\varepsilon_o n'_{s\perp}$ which leads to:

$$\varepsilon_s \varepsilon_o (\varepsilon_o - \varepsilon_s) = (\varepsilon_o + \varepsilon_s) (\varepsilon_o - \varepsilon_s) n_x^2 \quad \frac{\varepsilon_s \varepsilon_o}{(\varepsilon_s + \varepsilon_o)} = n_x^2 \quad (38-39)$$

Equation 39 is once again the degenerate 2-phase equation seen before. If n_s is real and $n_{a\perp} \rightarrow i n'_{a\perp}$ then the degenerate solution occurs at the overlayer-ambient interface instead.

2.6.4 Case 4: All are Imaginary

The final case includes all of the indices of refraction as imaginary expanding equation 20 to:

$$0 = -\varepsilon_o n'_{o\perp} (\varepsilon_s n'_{a\perp} + \varepsilon_a n'_{s\perp}) \cos(hk'_{o\perp} d) - (\varepsilon_o^2 n'_{a\perp} n'_{s\perp} - \varepsilon_a \varepsilon_s n'^2_{o\perp}) \sin(hk'_{o\perp} d) \quad (40)$$

The solution can be found if d is once again zero leading to $\varepsilon_s n'_{a\perp} = -\varepsilon_a n'_{s\perp}$

which once again leads to $\frac{\varepsilon_a \varepsilon_s}{\varepsilon_a + \varepsilon_s} = n_x^2$ which is again the degenerate

solution and since d is going to zero there is no overlayer.

2.7 Conclusion

Based on the Drude Free Electron Model and the Fresnel equations a theoretical model for the calculations of the SPP was derived. This model can be used for comparing theoretical and experimental data as well as understand on a mathematical and physical level the events that lead to the excitation of the plasmon. Through the exploration of the poles the exact conditions that govern the appearance of the surface plasmon were explored. The treatment resulted in a waveguide solution where the standard surface plasmon where the waveguide has zero thickness plasmon where n_a and n_s are imaginary and n_o is real. An electrostatic solution for an imaginary n_o and small n_x and a degenerate 2-phase solution exists for an imaginary n_a or n_s and an imaginary n_o and for all n 's imaginary.

Chapter 3 Materials and Methods

3.1 Surface Plasmon Resonance Data Collection

The SPP data was collected on a Surface Plasmon Resonance attachment to a 6700 Nicolet FT-IR. Detector used is an extended range, from mid to near IR, and an indium gallium arsenic detector, InGaAs. The SPR 100 uses a Kretschmann configuration (Figure 2A) and θ - 2θ stage. The sample is placed conductive side, ITO side, down into the sample holder. The BK7 glass prism is coated with index-matching fluid on the glass before the prism is placed on top. The prism is tightened with a wedge holder and screw and is then placed on the stage. For each sample a total of 32 scans were collected at each angle for a total of 31 angles ranging inside the prism from 41.5° to 52° . For each sample both s and p-polarized light was collected at a resolution of 4 cm^{-1} .

The carrier concentration and mobility measurements were performed on a Ecopia HMS-3000 Hall effect measurement system. Dektak profilometer was used to determine the thickness of the thin films.

3.2 Overlayer Preparations

3.2.1 Carrier Concentration Series for ITO on BK7 glass

The thin films used in these experiments were prepared by Mark Losego at North Carolina State Universities Department of Material Science and a detailed procedure of this can be found in Losego et al. [6]. A precise description

of the overlayer preparation for the carrier concentration and mobility series can be found in Losego et al. [6]. The annealing process was performed in a 5% H_2 and 95% N_2 forming gas with a partial pressure of 10^{-24} mTorr of O_2 and a second time with varying O_2 pressures for 6 different samples of 7×10^{-7} , 1×10^{-5} , 1×10^{-4} , 1×10^{-2} , 1, and 50 mTorr.

3.2.2 Mobility Series for ITO on BK7 glass

The Argon sputtering pressure was varied from 7mTorr, 10mTorr, 15mTorr, to 20mTorr. Hall Effect measurements were done to find the carrier concentration of each sample and the reported thickness is approximately 150nm. [6]

3.2.3 Overlayer Preparation on Silicon

ITO was deposited on series of silicon substrates that varied as a function of sputtering pressure and the annealing temperature. The two pressure series were deposited using RF sputtering at varying Argon gas pressure ranging from 6mTorr to 20mTorr. The sputtering target was 2.375 inches away from the substrate and the power was 20W. All samples were deposited at room temperature for ~ 23 minutes for the hexadecanethiol series and ~30 minutes for the octadecylphosphonic acid series and were then annealed at a temperature of 500°C for 30min in 5% H_2 forming gas. As the pressure of the Argon gas increases so did the surface roughness. A second series was deposited at room

temperature for ~20 minutes at a power of 20 Watts at an Argon pressure of 8.5mTorr. The substrates were then annealed at varying temperatures ranging from 100°C to 500°C in order to further understand how different roughness can be achieved. The roughness increases proportional to the annealing temperature. The substrates were annealed for 30 minutes each in 5% H₂ forming gas except for an amorphous sample, which was not influenced after the initial deposition. Both sets of samples have an approximate thickness of 150 nm.

3.3 Monolayer preparation

3.3.5 Hexadecanethiol

Hexadecanethiol (C16-SH) deposition was performed on both sets of samples in order to investigate the dependence of ordering of self-assembled monolayers on varying surface conditions. Depositions done for NEXAFS experiments were performed at Brookhaven National Lab. All samples were cleaned using UV-Ozoneolysis for 5 minutes in a UVO-cleaner UVO-60, model number 42, Jelight Company, Inc. immediately prior to monolayer deposition. The samples were then immediately submerged in a solution of neat hexadecanethiol between 14-18 hours with the least possible exposure to light and air. The samples were then cleaned using generous amounts of ethanol and dried with nitrogen gas. NEXAFS experiments were performed within an hour of the sample cleaning with minimal exposure to light and air.

3.3.6 Octadecylphosphonic Acid

Octadecylphosphonic acid deposition was performed on a pressure series similar to the one used for hexadecanethiol deposition. All samples were made at North Carolina State University and all depositions were performed at Brookhaven National Laboratory. All samples were cleaned using UV-Ozoneolysis for 5 minutes in a UVO-cleaner UVO-60, model number 42, Jelight Company, Inc. immediately prior to monolayer deposition. After ozoneolysis the samples were allowed to sit for ~ 12 hours in a 1 mM octadecylphosphonic acid solution diluted with EtOH. After depositions the samples were cleaned using EtOH and within the hour NEXAFS experiments were performed to insure minimal exposure to air.

3.4 Near-edge x-ray absorption fine structure (NEXAFS) Spectroscopy

NEXAFS experiments were performed at the BIST/Dow Soft X-ray Materials Characterization Facility at the National Synchrotron Light Source at Brookhaven National Lab (NSLS-BNL) on the U7A beam line using a partial electron yield (PEY) intensity detector (grid bias of -150V) and a charge compensation of 25 μ A. The NEXAFS data was collected for six separate angles of incidence (20° , 30° , 40° , 55° , 70° , and 90°) for the hexadecanethiol samples and for seven angles for the octadecylphosphonic acid samples (20° , 30° , 40° , 55° , 70° , 80° , and 90°) for a photon energy range of 260-390 eV. The incident angle was varied in order to determine the orientation of the molecules on the surface. The highest scan rate used, 0.1eV per 1 second was between 285-

295eV for all samples due to the C-H bond excitation and the C-C bond excitation. All NEXAFS studies performed focused on these two transitions.

3.5 Atomic Force Microscopy

AFM (Atomic Force Microscopy) measurements were conducted by Nanosurf Easy Scan 2 in tapping mode in order to determine the structure of the surface.

Chapter 4 Experimental and Theoretical Results and Comparison

4.1 Introduction

In order to explore the dependence of the surface plasmon effect, material parameters such as film thickness, charge carrier density and mobility on ITO thin films permitted three independent parameters to be systematically varied. The film thickness was controlled by changing the deposition time. The electron mobility was altered by changing the Argon gas sputtering pressure. The charge carrier concentration was varied by changing the pressure of the forming O₂ gas during the post-annealing process. The experiments presented here were conducted on ITO thin films deposited on BK7 glass. The appearance of the surface plasmon is highly dependent on the thickness of the conducting layer as shown in Figure 7. In order to vary the thickness parameter of ITO the deposition time of the thin films was controlled while all other parameters such as target distance, targeting gas pressure, temperature, and forming gas pressure, remained constant.

4.2 Effect of Film Thickness

Films up to 70nm thickness have a reflectance decrease attributable to the screened bulk plasmon polariton (SBPP). The SBPP in ITO can be observed as a narrow dip in the near infrared spectral region at around 9000 cm⁻¹ with a weak angle dependence. The surface plasmon polariton (SPP) is observed in films of thicknesses greater than 70 nm. Unlike the SBPP, the SPP wavenumber

depends strongly on the angle of incidence. For the thickness series shown in Figure 7 the SPP appears starting at around 6500 cm^{-1} for the highest incident angle, 52° , and is found at around 4500 cm^{-1} for the lowest angle collected at 42° . The 160 nm thick film shows the greatest decrease in reflected intensity and is therefore the optimum thickness for the SPP. The SPP starts to decrease as the thickness of the thin films is increased beyond 160 nm. However, the high energy Fabry-Perot anti-resonance becomes more pronounced in thicker films. [7] While thickness dependence of the SPP is an extremely useful physical feature, the study of the electronic properties of ITO thin films was also performed. The appearance of the surface plasmon is dependent on ω_p or the plasmon frequency described by equation 2.

4.3 Effect of Carrier Concentration

In ITO, the charge carriers are created by oxygen vacancies or doping of Sn to create extra electrons in the lattice. The charge carrier concentration, n , has an easily predicted effect on the plasma frequency; ω_p . Observation of the SPP provides a direct measure of the relative value of ω_p permitting a comparison of theory to experiment. During the second annealing process the partial pressure of oxygen was increased to permit a controlled decrease in the charge carrier concentration of the thin films. The change in carrier concentration can be attributed to the filling of holes by the oxygen. As oxygen fills the vacancies it complements the Sn coordination sphere to trap electrons. With the

decreasing of carriers the carrier concentration decreases as shown in Figure 5 for a series of ITO thin films.

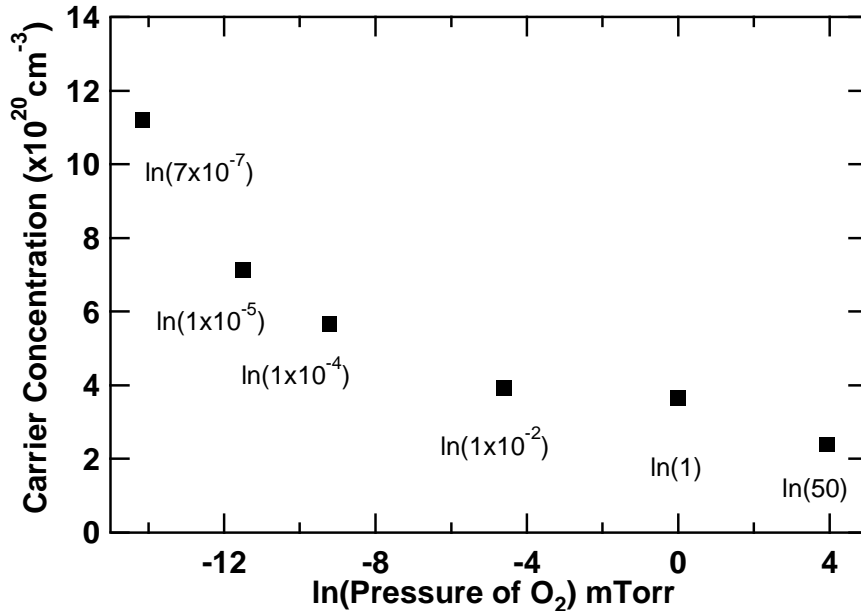


Figure 5 The graph of $\ln(\text{pressure of oxygen gas})$ during the post annealing process versus the carrier concentration determined by Hall Effect Measurement. Each of the original pressures is listed next to the appropriate data point.

4.4 Effect of Electron Mobility

The electron mobility can be controlled by varying the sputter gas pressure as shown in Figure 6. Electron mobility has an inverse relation to the damping constant γ , $\Gamma = e/(\mu m_e)$, and therefore to the width of the SPP as shown in the comparison in Figure 10. Figure 6 shows that as the sputtering pressure increases to 9 mTorr or decreases from 9 mTorr the mobility of the thin film decreases. The greatest mobility of the series is for a target gas pressure of

9 mTorr at $30.0 \text{ cm}^2/\text{Vs}$ for which the surface highest polariton appearing at 6000 cm^{-1} as shown on Figure 3. The change in electron mobility affects the width of the SPP peaks. It is clear from Figure 6 that as the sputtering pressure moves away from 9 mTorr the width of the peaks increases.

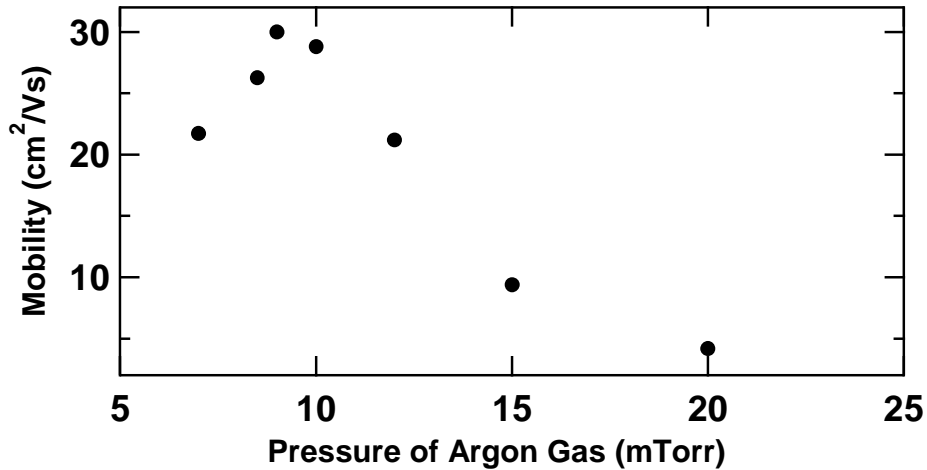


Figure 6 The graph of seven substrates with target gas pressure of 7mTorr, 8.5mTorr, 9mTorr, 10mTorr, 12mTorr, 15mTorr, and 20mTorr versus the measure mobility of each.

4.5 Experimental Data Compared to Theoretical Data

4.5.1 Thickness Series

In order to calculate the theoretical curves the experimental parameters such as carrier concentration, mobility and the varying thickness were used. The carrier concentration and mobility data was acquired using a Hall Effect probe. The calculations for the thickness series used $1 \times 10^{27} \text{ cm}^{-3}$ for the carrier concentration, $4 \times 10^{-3} \text{ m}^2/(\text{Vs})$ for the mobility, and varied the thickness. Figure 7

A-D shows the experimental data and E-H shows the corresponding theoretical calculations.

Although the theoretical predictions show the SPP to be lower than the experimental, this could be due to the approximation of the effective mass, the general curve of the SPP, the screened bulk plasmon, and the high energy anti-resonance is the same in both theoretical and experimental data. The thicker films can be seen in Figure 8 M-O for experimental P-Q for the theoretical.

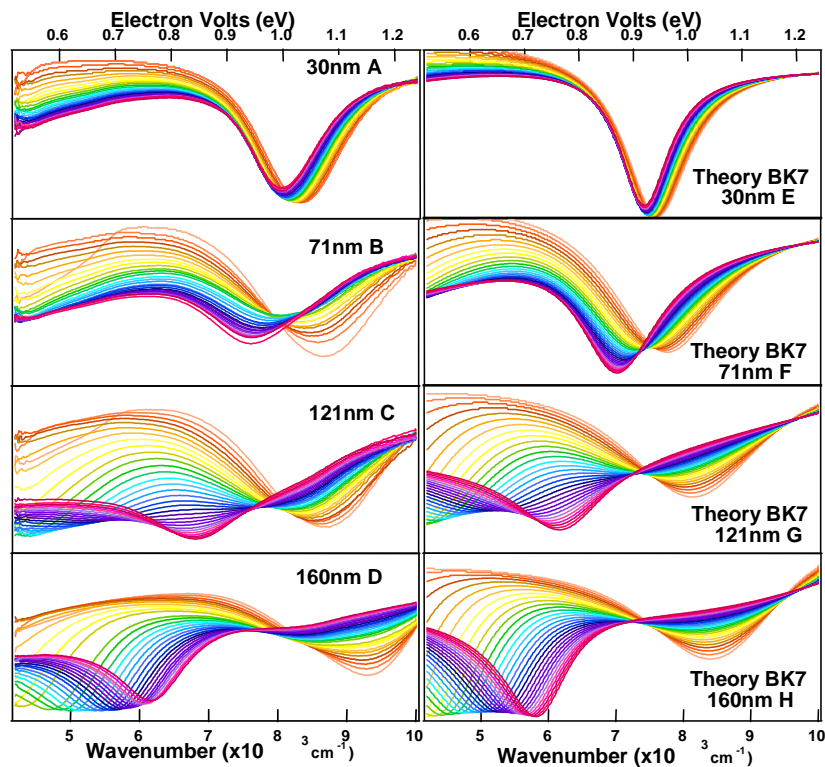


Figure 7 Experimental data (A-D) collected showing varying thickness of ITO on BK7 glass, theoretical calculation for the series (E-H).

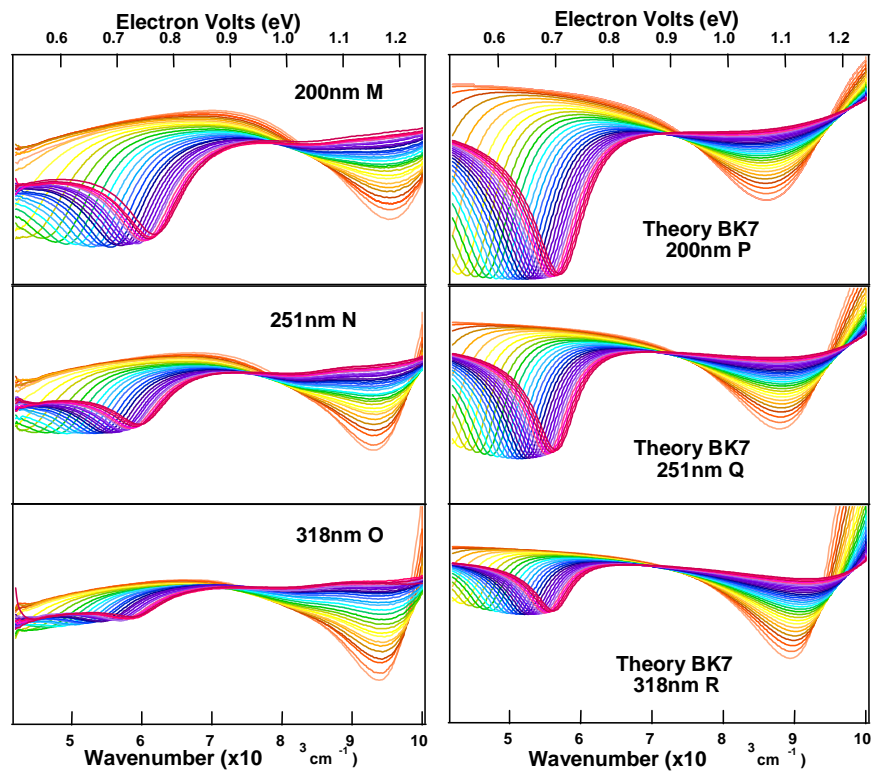


Figure 8 Experimental data (M-O) collected showing varying thickness of ITO on BK7 glass, theoretical calculation for the series (P-R).

4.5.2 Carrier Concentration

Carrier concentration is controlled by changing the pressure of oxygen during the annealing process. Figure 9 shows the experimental and theoretical data for this series. The left column represents the experimental data where while the right column represents the corresponding theoretical calculations. The furthest right peaks on each of the graph represent the highest incident angle measured, as the angles decrease, purple is 52° and moving down to orange at 42° , the polariton peaks move towards the mid-IR. The exact position for the

polariton in graph A is not known because it moves out of the range of the instrument and into the mid-IR. These graphs clearly show that a slight change in the partial pressure of oxygen from 10^{-7} to 10^{-5} , graphs D and C, move the polariton peak a thousand wavenumbers. The theoretical graphs show a general agreement with the experimental data of the shape of the SPP curves and the location of the peaks for the carrier concentration series. In Figure 9 E-H as the pO_2 is decreased the SPP shifts to the left, to the mid-IR region just like the experimental data. Although the agreement between the theoretical and experimental data is excellent there are slight visible differences. These discrepancies can be attributed to effective mass, since filling of vacancies by the oxygen will influence the effective mass of the thin film therefore should be slightly different from one to the next. The figure shows that the agreement between the thin films with a lower carrier concentration is better than that of higher carrier concentration, where the lower carrier concentration films have a closer effective mass to 0.4 than the higher carrier concentration films.

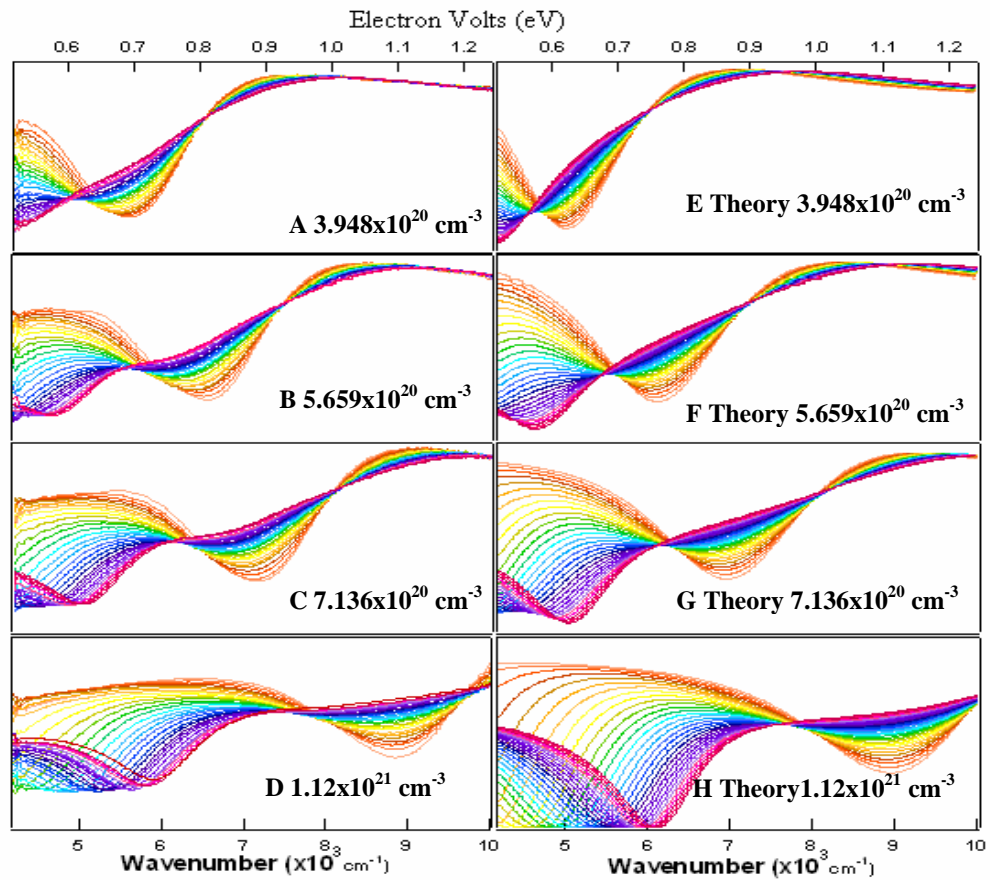


Figure 9 The experimental and theoretical data for the carrier concentration series. The partial pressure of oxygen for A and E is 0.01 mTorr, B and F 10^{-4} mTorr, C and G 10^{-5} mTorr, and D and H 10^{-7} mTorr.

4.5.3 Mobility Series

The pressure of the target gas Argon varies the mobility of the thin films. Although it is not entirely clear the exact reason for this one possibility is the change in the crystallinity of the thin films. As the pressure of the gas increases the higher pressure of the argon gas can cause greater concentration of defects

in the thin films. As mentioned by Losego et al. possible scattering sites in the lattice include grain boundaries, linear defects (dislocations), ionized impurities, or other point defects (implanted Ar impurities). The greater amount of defect influences the mobility since mobility is directly proportional to relaxation time and inversely proportional to the damping constant as the mobility decreases the damping constant increases widening the polariton peaks. Furthermore, Losego theorizes that the bandwidth is inversely proportional to mobility and as the mobility decreases the bandwidth increases causing wider peaks. (6)

Figure 10 shows that at 15 mTorr, graph D, the width of the peaks spans over 3000 cm^{-1} into the mid-IR while for 9 mTorr the peaks are not more than 2000 cm^{-1} in width. The width of the SPP band increases with an inverse proportionality to the mobility. In Figure 10 both the theoretical and experimental data show a broadening of the peaks as the pressure of Argon gas decreases below 9 mTorr or increases above 9 mTorr. The comparison of different series theoretical to experimental data shows how the general curve and the behavior of the SPP and other features are the same.

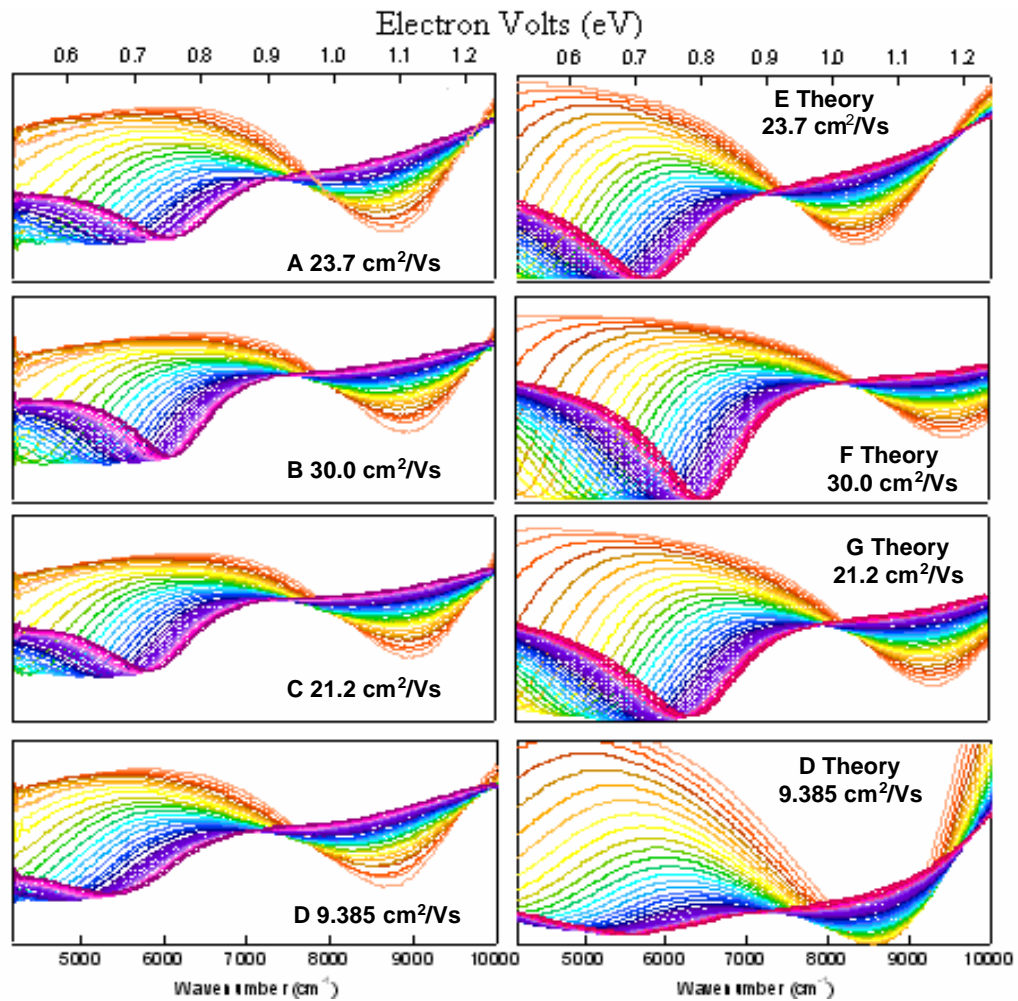


Figure 10 Varied pressure of the targeting gas changes the mobility cause a greater peak width. Where the sputtering pressure of the target gas is 6 mTorr for A and E, 9 mTorr for B and F, 12 mTorr for C and G, and 15 mTorr for D and H.

4.5.4 Influence of Substrate Index of Refraction on SPP

In order to understand the influence of the glass used in the deposition of the thin films the thickness series was calculated using SF10 glass which has a higher index of refraction than BK7 (BK7:1.52, SF10:1.72). The calculations for

SF10 glass are shown in Figures 11 I-L and Figure 12 S-U, each in a row with corresponding theoretical and experimental graphs of the same thickness on BK7 glass. The SF10 36 SPP are narrower than the corresponding BK7 data and the plasmon dip spacing is closer than that of the SPP in BK7 glass. Also the high energy anti-resonance feature is almost not existent in the SF10 glass.

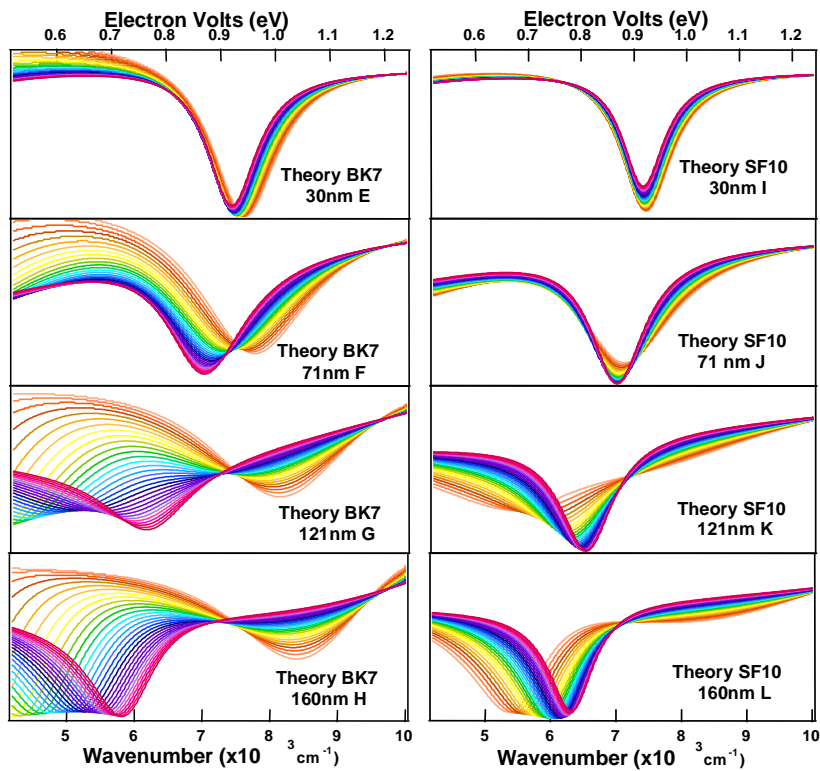


Figure 11 Comparison of substrates, BK7(left) vs SF10 (right) glass.

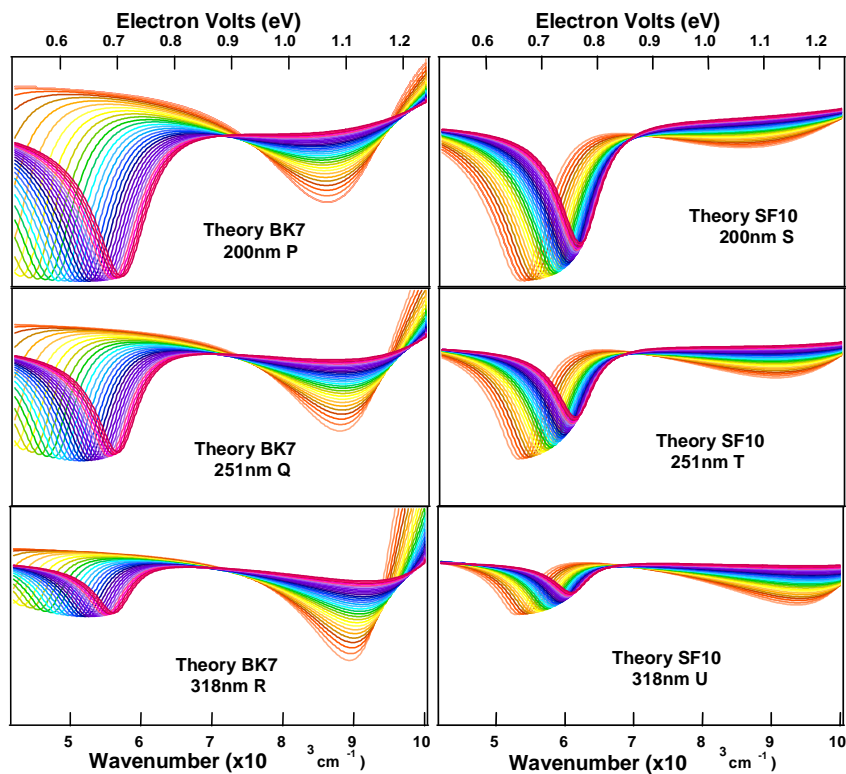


Figure 12. Comparison of substrates, BK7 vs SF10 glass.

4.6 Exploration of Different Substrates; Consideration of the Generality of the SPR Effect for Conducting Metal Oxides

Although most studies to this point have been conducted using ITO, the observation of surface plasmons is predicted to be a general feature of CMOs. Materials of interest include cadmium tin oxide, CTO, aluminum zinc oxide, AZO, fluorine doped tin oxide, SFO, iridium oxide, and ruthenium oxide. Some of these conducting metal oxide thin film materials are expected to have similar behavior to ITO with the plasmon appearing in the near-IR. AZO has a lower high

frequency dielectric constant, $\epsilon_{\infty} = 3.24$, and a smaller effective mass than ITO, 0.28 vs. 0.4, which influences the carrier concentration since fewer carriers are present in the thin film. Therefore the expected appearance of the plasmon in AZO would be lower than ITO. SFO on the other hand has a similar effective mass and slightly higher carrier concentration but greater sheet resistance than ITO, which influences the relaxation time to be lower than that of ITO and causes broader peaks. Furthermore CTO is a very similar substrate to ITO, with carrier concentration, sheet resistance, relaxation time similar to ITO, but a high frequency dielectric twice as large as ITO, 6.76 compared to 3.8. This dielectric value permits a much lower appearance of the plasmon in the mid-IR range. All these substrates are shown in Figure 13, as is ITO for comparison. Figure 14 shows the dispersion curves for ITO, CTO, and AZO. The dispersion curves are based on a two-phase model, used in the theoretical calculations above, with one interface having a refractive index of 1.5 and only the real part of equation 3 is graphed, shown by the blue curves. A light line, 70° , and the equation used to calculate it is also shown on the graphs. The light line intersects the SPP curve where coupling occurs and the SPP is driven. The prediction of AZO in Figure 14 is around 4000 cm^{-1} which is slightly lower than the theoretically calculated SPP curve. Furthermore, the same is seen for CTO for which the dispersion curve predicts the SPP to be around 2500 cm^{-1} and the theoretically calculated CTO SPP curve begins to appear slightly below that. The dispersion curve for ITO is

also shown for comparison and predicts the SPP dispersion to be around 5900 cm^{-1} which is where the theoretically calculated SPP is seen in Figure 14.

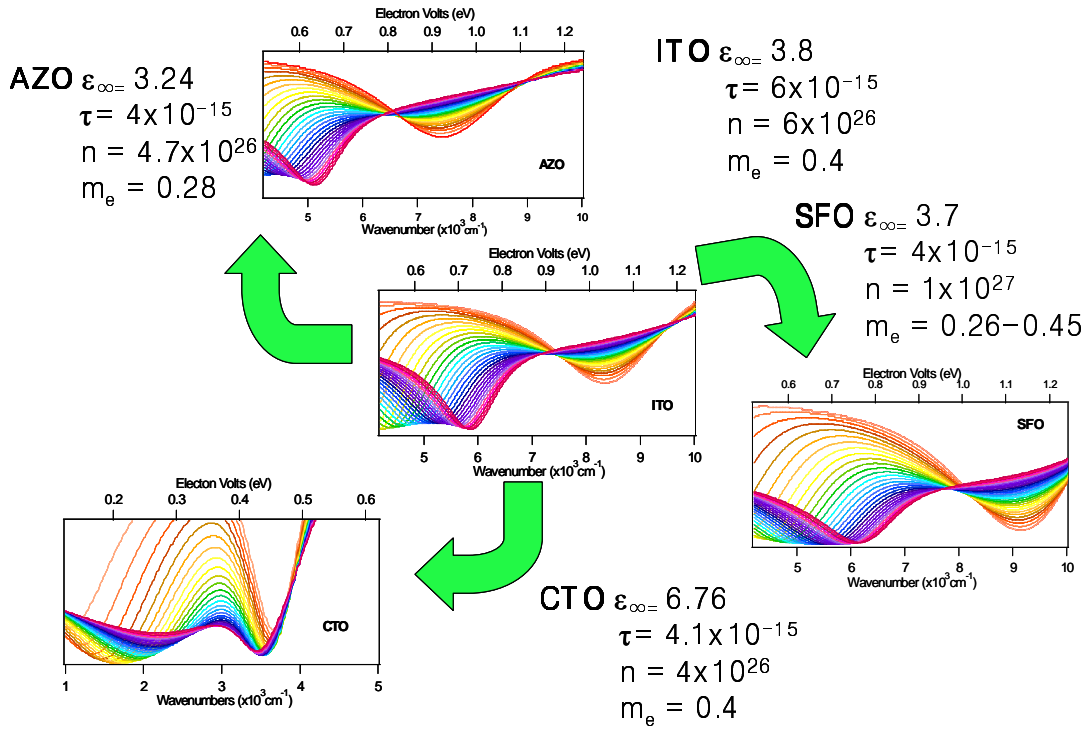


Figure 13 Theoretical Calculations for AZO, SFO, and CTO compared to ITO.

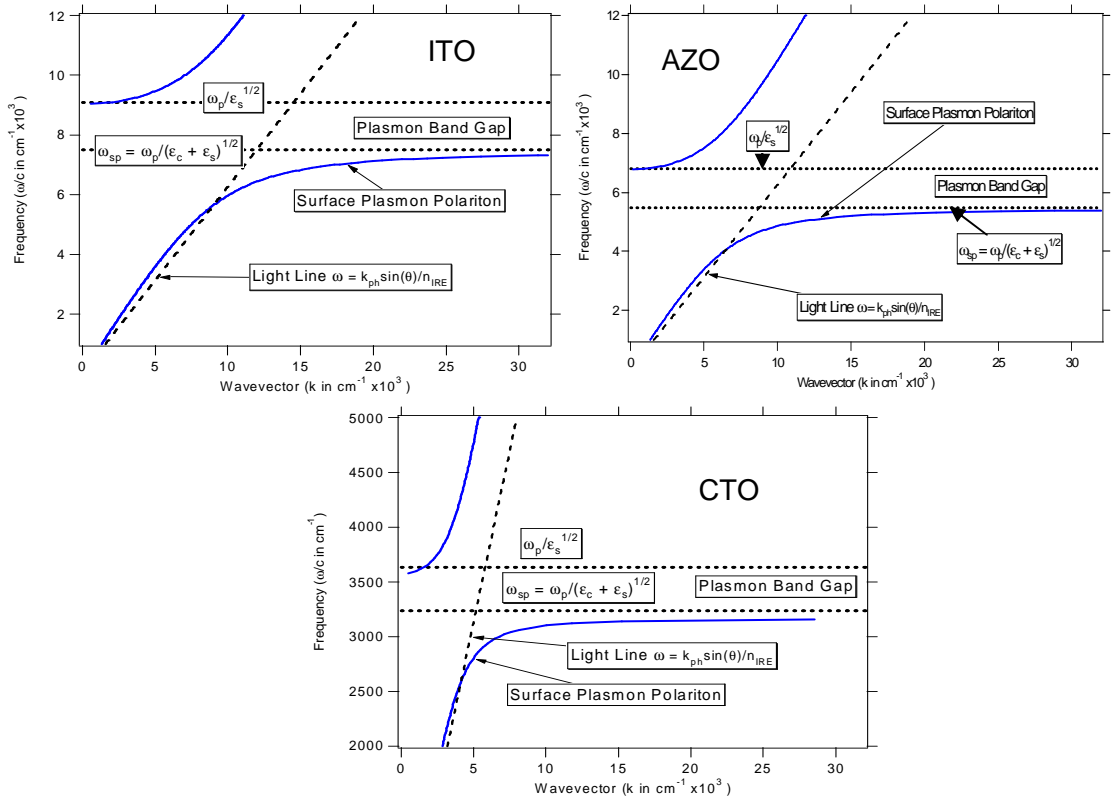


Figure 14 Dispersion curves for ITO, AZO, and CTO.

4.7 Conclusion

The exploration of the variable parameters of ITO leads to a better understanding of the SPP response. With the use of variable deposition time it was found that the SPP appeared for thicknesses greater than 70 nm, with the optimal thickness for the SPP response at around 150-160 nm. Additional

deposition time increased the thickness and decreased the intensity of the SPP and increased the intensity of the Fabry-Perot anti-resonance response.

The electrical properties of ITO allow for the tuning of the SPP response in order to achieve the best spectra possible. By varying the partial pressure of oxygen and allowing it to fill in the vacancies, the carrier concentration can be systematically varied. The plasma frequency has a square root dependence on the carrier concentration; therefore as the carrier concentration increases so does the plasma frequency. As the partial pressure increases, from 10^{-7} mTorr to 0.01 mTorr, the carrier concentration decreases and the SPP peak shifts into the mid-IR, from 6000 cm^{-1} to below 4200 cm^{-1} . The mobility of the thin films can be varied by adjusting the pressure of the target gas, Argon. As the pressure moves away from 9 mTorr the mobility and therefore the relaxation time which is directly proportional to mobility decrease. This leads to the broadening of the SPP peaks.

The experimental data were compared to the theoretical calculations. The model used the same measured parameters as the experimental data for charge carrier density, thickness, and mobility. These were the only adjusted parameters in the calculations. The specific measurements for each of the samples were collected experimentally. There are no other adjustable parameters and no there was no manipulation of the data after the calculation was performed. It was found that the general trends in all the series were the same and the experimental data overall matched the theoretical calculations quite well. This encourages the use

of this model for calculating other CTO and their SPP response in order to make new thin films.

Chapter 5 Near Edge X-ray Absorption Fine Structure Spectroscopy of Self Assembled Monolayer on Indium Tin Oxide Thin

5.1 Introduction to NEXAFS

Near Edge X-ray Absorption Fine Structure Spectroscopy is used to study the orientation of self-assembled monolayers (SAMs) on thin film surfaces. A low intensity absorption x-ray beam is used to excite K or L shell ground state electrons into the unoccupied antibonding orbitals. The excitation results in an unoccupied hole, which is filled by an electron from an outer shell. The decay of the outer shell electron results in the release of energy, which is absorbed by another outer shell electron, which results electron ejection.. This second ejected electron is referred to as an Auger electron. The excitation of a core electron results in different spectral features depending on the bonds present on the surface of the substrates. The C-H ground state to antibonding transition ($1s \rightarrow \sigma^*$) occurs at around 287.6 eV while the broader C-C transition ($1s \rightarrow \sigma^*$) occurs around 293.1 eV. Since the $1s \rightarrow \sigma^*$ transition moments for the C-H and C-C molecular orbitals are approximately orthogonal to one another there is usually a trade-off in intensity as a function of the angle of incidence of the polarized X-ray beam to the thin film. By extracting the intensity of both bands as a function of angle of incidence it is possible to determine the orientation of the molecules on the surface. Furthermore, the intensity of the peaks depends on

the orientation of the bonds due to the X-ray beam. When the X-ray beam is parallel to the antibonding orbitals the intensity of the peak is much greater than in those antibonding orbitals, which are perpendicular to the x-ray beam.

5.2 Normalization of the Data

The raw data are normalized by dividing the partial electron yield (PEY) NEXAFS signal by the ionization energy (IO). The PEY NEXAFS uses a minimal energy threshold, which only utilizes electrons that have a kinetic energy greater than electron potential, E_p . The normalization is performed by first setting the pre-edge to zero at 280 eV and was adjusting the post-edge at 320 eV one.

5.3 Hexadecanethiol Orientation

The normalized data are then plotted for the grazing (20°), magic (55°) and normal (90°) angles for the hexadecanethiol data, Figures 15 and 16. The 20° angle is to the closest to grazing incidence. The difference plots are produced to determine if there is orientation in the SAMs. This is done by subtracting the grazing from the normal angles to create a difference plot of the data. The normal angle accounts for one extreme of the x-ray beam orientation to the molecule while the near-grazing angle accounts for the other extreme. Differences in the intensities in the spectrum result from the orientation of the molecules on the surface as explained above.

In order to understand how the parameters of the SAM film are influenced by the surface roughness, pressure, and annealing during the substrate preparation, a

series of SAMs was prepared on neat hexadecanethiol. Silicon was used as a substrate because it is molecularly smooth. The pressure series consists of samples prepared with variations in the sputtering pressure of the Argon gas as follows: 6, 7, 8.5, 10, 15, and 20 mTorr. Figure 15 shows the PEY NEXAGS spectra collected at the grazing (20° , green), normal (90° , black), and magic (55° , blue), angles for each of the samples a-f. As the sputtering pressure of the target gas increases so does the surface roughness of the samples. Figure 15 shows that the greatest difference plots exist for sputtering pressure of 8.5 and 10 mTorr which have a surface roughness of 1.7 and 2.0 nm, respectively. The second series includes the effect of changing the temperature during the annealing process, cf. Figure 16. For 100°C and the amorphous samples the difference plots exhibit the largest peaks in the NEXAFS difference plots. As the temperature increases the roughness also increases resulting in a smaller differential signal. The surface roughness of a specimen prepared at 100°C and that of an amorphous sample is lower than both of the best samples in the pressure series. However, the differences plots exhibit the largest peak differences for specimens possessing much lower surface roughness. It can be assumed that it is the change in crystallinity due to different annealing temperatures that causes the surface to be less accommodating for the SAM deposition. Furthermore, while sample c of the pressure series and f of the annealing series have the same conditions, sample c has a surface roughness of 1.7 nm and specimen f possesses the roughness of 1.0 nm. This difference in

surface roughness has a great effect on the deposition of the SAMs as sample c has much more ordered SAMs and sample f has almost none. As a result it is clear that a combination of sputter pressure and annealing temperature can be used in order to make thin films with favorable conditions for oriented adlayers.

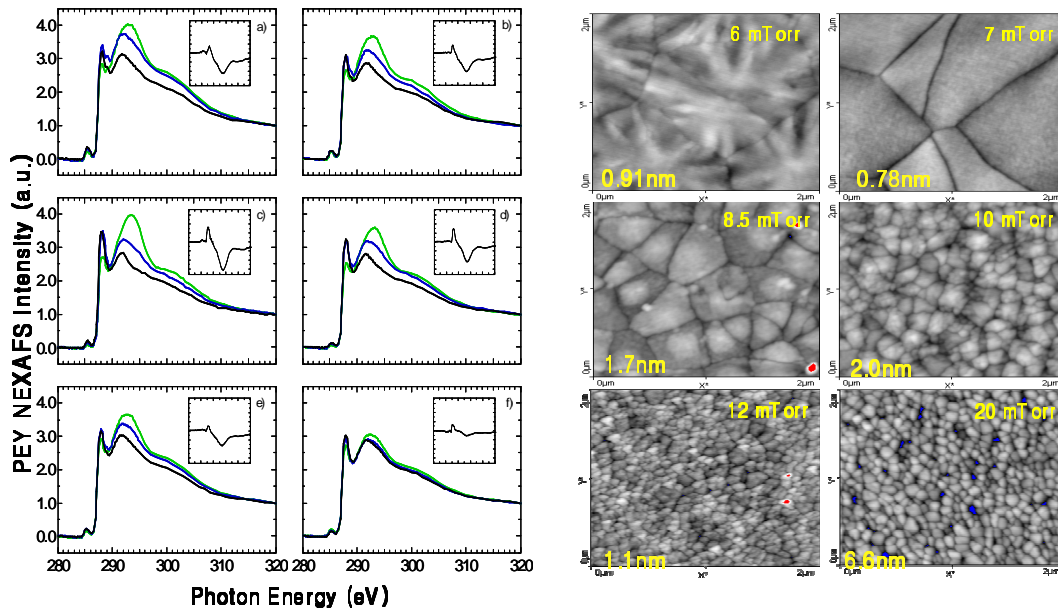


Figure 15 The pressure series of ITO on Silicon. The AFM data on the right corresponds in location to the NEXAFS data on the left. The difference plots are located in their corresponding graphs. A) 6 mTorr RMS 0.91 nm B) 7 mTorr RMS 0.78 nm C) 8.5 mTorr RMS 1.7 nm D) 10 mTorr RMS 2.0 E) 12 mTorr 1.1 nm and F) 20 mTorr 6.6 nm. The green lines are the grazing at 20° , black is the normal at 90° , and blue is the magic at 55° .

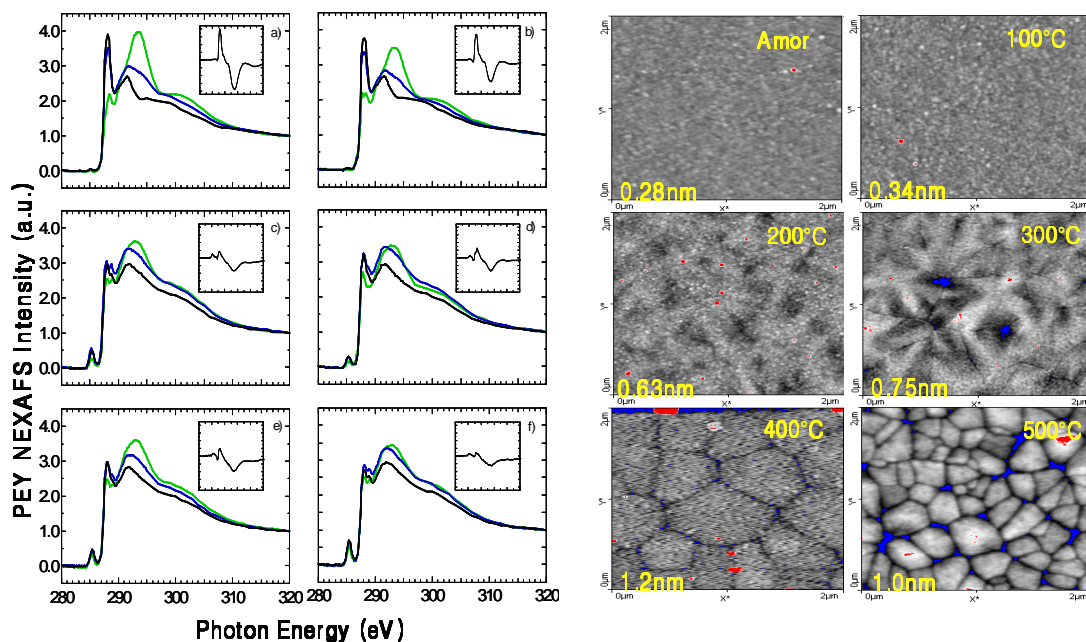


Figure 16 The annealing series of ITO on Silicon. The AFM data on the right corresponds in location to the NEXAFS data on the left. The differences plots are located in their corresponding graphs. A) Amorphous RMS 0.28 nm B) 100°C RMS 0.34 nm C) 200°C RMS 0.63 nm D) 300°C RMS 0.75 nm E) 400°C 1.2 nm and F) 500°C 1.0 nm. The green lines are the grazing at 20°, black is the normal at 90°, and blue is the magic at 55°.

5.4 Calculating Tilt Angles

In order to calculate the tilt angles for phosphonic acid SAMs, the NEXAFS spectra were fitted to a series of Gaussian curves using an Excel macro by following the NEXAFS analysis procedure described in Outka (7). The macro generates a difference NEXAFS spectrum, which allows for identification of peaks present in the sample, including their positions and widths. A background spectrum is generated by matching the peak heights of one of the experimentally-measured NEXAFS spectrum (typically that collected at the

“magic” angle) to the calculated one. This background spectrum is then used to interpret NEXAFS spectra of each angle collected from the same specimen in conjunction in the fitting procedure that adjusts the heights of each NEXAFS signal identified in the difference spectrum in order to achieve the best match between the calculated and the experimental NEXAFS spectrum. The areas of each peak obtained by fitting every angular NEXAFS spectra are then used to generate a normalized plot to which the tilt angles calculated using the procedure outlines in the supplementary material section of ref. 8.

5.5 Phosphonic Acid Tilt Angles

The pressure series with octadecylphosphonic acid on ITO/Si was evaluated for tilt angles using the procedure described above. Examples of the fitted data for angles 20 and 90 are in Figure 17 and the generated tilt angle graph is in Figure 18, both are for a sample with Argon pressure deposition at 6 mTorr. The peak areas are graphed and compared to the different tilt angles calculated for specific angles depicted in the graph. The experimental NEXAFS data were interpreted using the tilt model developed by Outka and coworkers [7]. By comparing the experimental data to the predicted NEXAFS intensities, the approximate tilt angle of the chain is determined. This fitting is done for the remainder of the series listed in Table 1.

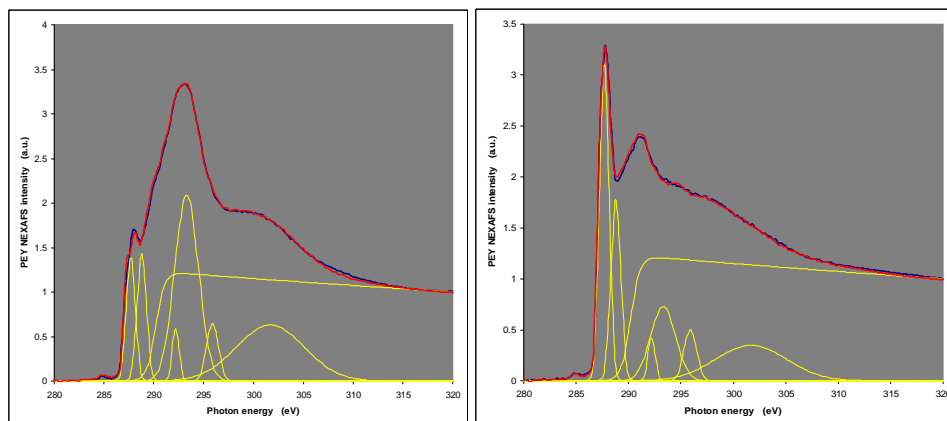


Figure 17 Example of fitted data. The blue line underneath the red is the normalized experimental data while the red is the summation of the adjusted intensities identified by the difference spectra shown in yellow. The graphs shown are for sample out of the pressure series, 6 mTorr. The graph on the left is at 20° and on the right is 90° .

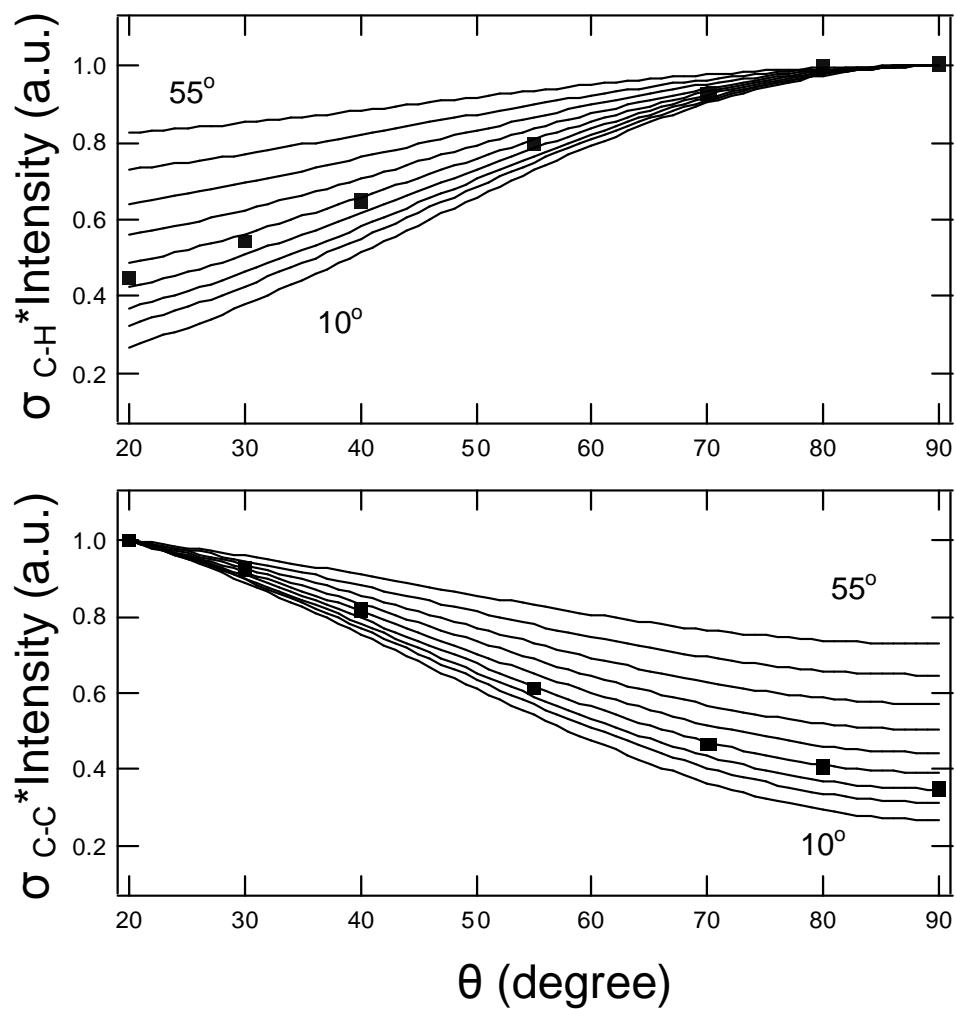


Figure 18 The top graph shows the peak area for the $1s \rightarrow \sigma_{C-H^*}$ and the bottom graph show the peak are for the $1s \rightarrow \sigma_{C-C^*}$. Each of the lines represents different chain tilt angles (starting at 10° , shown on graph, 20, 25, 30, 35, 40, 45, 50, 55, shown on graph) evaluated using Reference 7.

Table 1. The calculated tilt angles for the pressure series with octadecylphosphonic acid are shown.

Pressure (mTorr)	Chain tilt based on $1s \rightarrow \sigma_{C-H}^*$ (deg)	Chain tilt based on $1s \rightarrow \sigma_{C-C}^*$ (deg)
4	30 ± 5	10 ± 5
6	35 ± 5	35 ± 5
8	25 ± 5	20 ± 5
9	25 ± 5	10 ± 5
10	30 ± 5	30 ± 5
12	30 ± 5	30 ± 5
15	45 ± 5	45 ± 5
20	45 ± 5	20 ± 5

The phosphonic acid pressure series shows that for lower pressures the approximate orientation of the chains possesses the lowest tilt angles at 8 mTorr and 9 mTorr based on the $1s \rightarrow \sigma_{C-H}^*$ NEXAFS data. The tilt angle increases for any deviation of the sputter gas pressure from from 9 mTorr. For the $1s \rightarrow \sigma_{C-C}^*$ the molecule tilt angles are more irregular; the highest tilt angle is observed at 15 mTorr and the lowest tilt is detected at 9 and 4 mTorr. This supports the notion that the pressure of the Argon gas during the ITO deposition alters the morphology of the thin films causing a change in the tilt angles.

5.6 Conclusion

NEXAFS experiments were performed in order to test the propensity for well-ordered SAMs to form on ITO. By systematically changing the pressure of the Argon gas used in the ITO deposition, it was found that the tilt angles of the hexadecanethiol series varies. The most consistent title angles in

hexadecanethiol SAMs (25-45 deg) were found on ITO substrates prepared at pressures between 6 and 12 mTorr.

REFERENCES

- 1) Brockman, J. M.; Nelson, B. P.; Corn, R. M., *Surface plasmon resonance imaging measurements of ultrathin organic films*. Annual Review of Physical Chemistry 2000, 51, 41-63.
- 2) Homola, J.; Yee, S. S.; Gauglitz, G., *Surface plasmon resonance sensors: review*. Sensors and Actuators B-Chemical 1999, 54, (1-2), 3-15.
- 3) Knoll, W., *Interfaces and thin films as seen by bound electromagnetic waves*. Annual Review of Physical Chemistry 1998, 49, 569-638.
- 4) Franzen, S., *Surface plasmon polaritons and screened plasma absorption in indium tin oxide compared to silver and gold* 10.1021/jp7097813. Journal of Physical Chemistry C 2008, 112, (15), 6027-6032.
- 5) Brewer, S. H.; Franzen, S., *Indium tin oxide plasma frequency dependence on sheet resistance and surface adlayers determined by reflectance FTIR spectroscopy* 10.1021/jp026600x. Journal of Physical Chemistry B 2002, 106, (50), 12986-12992.
- 6) Losego, M. Efremenko, A. Rhodes, C. Cerruti, M. Franzen, S. Maria, J. *Conductive Oxide Thin Films: Model Systems for Understanding and Controlling Surface Plasmon Resonance* (Manuscript in progress)
- 7) Rhodes, C.; Cerruti, M.; Efremenko, A.; Losego, M.; Aspnes, D. E.; Maria, J.P.; Franzen, S., *Dependence of plasmon polaritons on the thickness of indium tin oxide thin films* 10.1063/1.2908862. Journal of Applied Physics 2008, 103, (9).
- 8) Cerruti, M.; Rhodes, C.; Losego, M.; Efremenko, A.; Maria, J. P.; Fischer, D.; Franzen, S.; Genzer, J., *Influence of indium-tin oxide surface structure on the ordering and coverage of carboxylic acid and thiol monolayers* 10.1088/0022-3727/40/14/016. Journal of Physics D-Applied Physics 2007, 40, (14), 4212-4221.
- 9) Outka, D.A. Stohr, J. Rabe, J.P. Swalen, J.D. *The orientation of Langmuir-Blodgett monolayers using NEXAFS* J. Chem. Phys. 88(6)4076-4087 1998

APPENDICIES

Appendix A Evaluating the Denominator for s-polarized Light

In order to understand what influences the rise of the anti-resonance peaks the denominator of the s-polarized light is explored. The calculations shown in the Appendix follow a similar process as for p-polarized light above. The electric field of the incident wave for s-polarized light is the denominator in equation 1, which is set to zero and equations 6 and 7 are then inserted for $r_{s,oa}$ and $r_{s,so}$:

$$r_s = \frac{r_{s,oa} + r_{s,so} e^{2ik_{o\perp}d}}{1 + r_{s,oa} r_{s,so} e^{2iko_{\perp}d}} = \frac{E_r}{E_i} = \infty \quad (1)$$

The mathematical calculations can be found in the appendix. Equation 2 is what in the rearrangement of the denominator of equation 1 and application of the Euler function yields equation 2 for s-polarized light:

$$0 = n_{o\perp} (n_{a\perp} + n_{s\perp}) \cos(k_{o\perp}d) - i(n_{o\perp}^2 + n_{s\perp}n_{a\perp}) \sin(k_{o\perp}d) \quad (2)$$

The above equation is then explored for different cases of each of the complex n . Each n can be real and imaginary for each of the three layers. In order to satisfy an appearance of the pole a solution that is found for the denominator must also not make the numerator vanish.

The first case explored is for all real n_o . The trivial solution to equation 2 is $n_o = 0$, however when this is the case in the denominator the same result is achieved in the numerator therefore this is not a solution. If on the other hand n_o is very small then the following solutions for Fresnel equations are achieved:

$$r_{s,so} = -\left(1 - \frac{2n_{o\perp}}{n_{s\perp}}\right) r_{s,oa} = \left(1 - \frac{2n_{o\perp}}{n_{a\perp}}\right) e^{2ik_{o\perp}d} = 1 + 2ik_{o\perp}d \quad (3-4)$$

When these equations are inserted into equation 14, in the main text, equation 5 is achieved. In equation 5 in order for the denominator to become zero n_a and n_s must be imaginary ($n_{a\perp} \rightarrow in'_{a\perp}$). This results in equation 6, however since this is light negative n_a or n_s cannot exist and the whole right side of the equation is positive. This results that for small n_o or $n_o = 0$ no solution is found.

$$r_{aos} = \frac{-\frac{1}{n_{a\perp}} + \frac{1}{n_{s\perp}} - i\frac{\omega d}{c}}{\frac{1}{n_{a\perp}} + \frac{1}{n_{s\perp}} - i\frac{\omega d}{c}} \quad (5), \quad 0 = \frac{1}{n'_a} + \frac{1}{n'_s} + 2\pi\frac{d}{\lambda} \quad (6)$$

The case two explores if n_o is real and non-zero while all other n 's are equal to zero. This result in equations 10 and 11, from the main text, to be 1 and -1, which leads to equation 14, in the main text, to be equal to:

$$r_s = \frac{-1 + e^{2ik_{o\perp}d}}{1 - e^{2ik_{o\perp}d}} = -1 \quad (7)$$

As e approaches 1 the above equation goes to zero and once again there is no pole.

In case three n_o is once again real and non-zero, n_a is real while n_s is imaginary. When these cases are applied to equation 2 the result can be divided into real and imaginary parts, equations 8 and 9. Once simplified and solved equation 10 can be solved using $n_o = 0$, but since that already has been

eliminated as a solution no solution is found for this case either. The same logic can be applied if instead of n_s is imaginary n_s is imaginary.

$$0 = n_{o\perp} n_{a\perp} \cos(k_{o\perp} d) + (n_{s\perp}' n_{a\perp}') \sin(k_{o\perp} d) \quad 0 = n_{o\perp} (n_{s\perp}') \cos(k_{o\perp} d) - (n_{o\perp}'^2) \sin(k_{o\perp} d)$$

$$0 = \frac{n_{o\perp}}{\cos(k_{o\perp} d)} \quad (8-10)$$

Case four once again uses a real non-zero n_o while all other n 's are imaginary, equation 11:

$$0 = n_{o\perp} (n_{a\perp}' + n_{s\perp}') \cos(k_{o\perp} d) - (n_{o\perp}'^2 - n_{s\perp}' n_{a\perp}') \sin(k_{o\perp} d) \quad (11)$$

However the solution to this exists in specific values of d , this is a waveguide and it is independent of all values of the n 's.

In case five the n_o is imaginary while all other n 's remain real. There is a possibility of a solution here if n_a and n_s are zero but the result is always one for any d so once again no pole exist:

$$r_s = \frac{-1 + e^{2ik_{o\perp}d}}{1 - e^{2iko\perp d}} = 1 \quad (12)$$

Case six is similar to three where instead of real n_o it is imaginary along with one of the other n 's. This again leads to a simultaneous solution of both the real and imaginary parts which leads to:

$$0 = \frac{-n_{o\perp}'}{\sin(k_{o\perp} d)} \quad (13)$$

Once again n_o is not zero and no solution is found. The last case, case seven, treats all the n 's as imaginary and n_o is once again non-zero. This is similar to case four where once again a solution is possible if n_a and n_s is zero but once again this leads to every solution for d to be one and no poles exist. Thus for s-

polarized light no solution can be found for the plasmons except for waveguide modes.

Appendix B Supporting Data for NEXAFS Calculations

The corresponding data to the fitted data shown for the 6mTorr pressure series sample of octadecylphosphonic acid on ITO. The “grazing” and “normal” angles for the rest of the series:

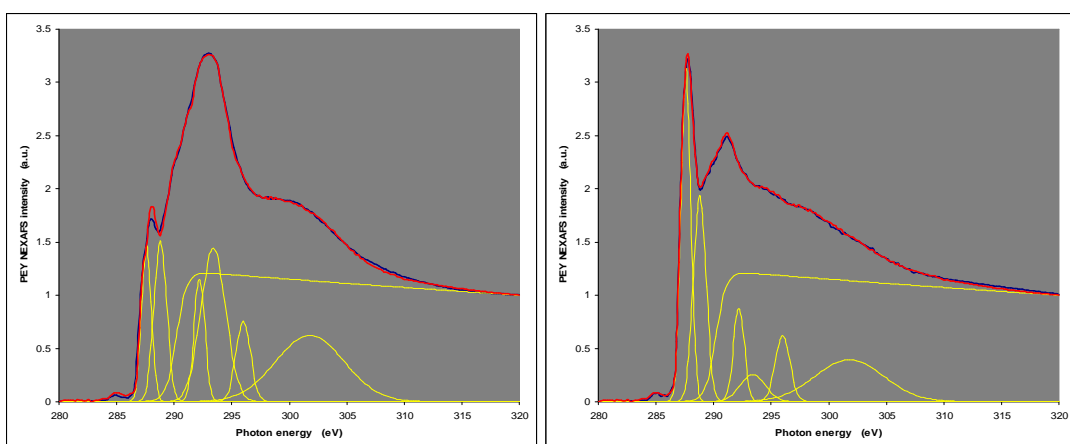


Figure 1. The fitted data for the 4mTorr sample of the pressure series with octadecylphosphonic acid on ITO/Si. On the left is the “grazing” angle 20° and on the right the “normal” angle 90° .

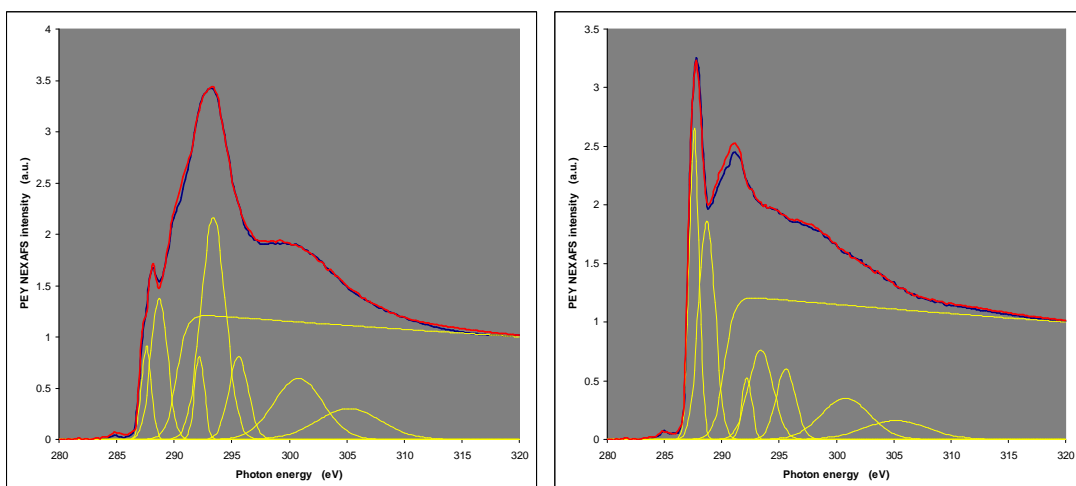


Figure 2. The fitted data for the 8mTorr sample of the pressure series with octadecylphosphonic acid on ITO/Si. On the left is the “grazing” angle 20° and on the right the “normal” angle 90° .

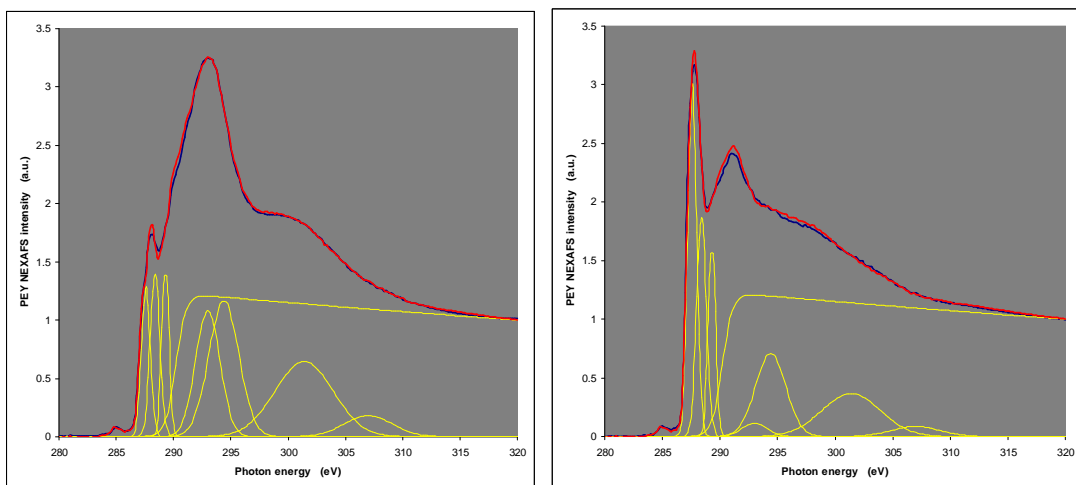


Figure 3. The fitted data for the 9mTorr sample of the pressure series with octadecylphosphonic acid on ITO/Si. On the left is the “grazing” angle 20° and on the right the “normal” angle 90° .

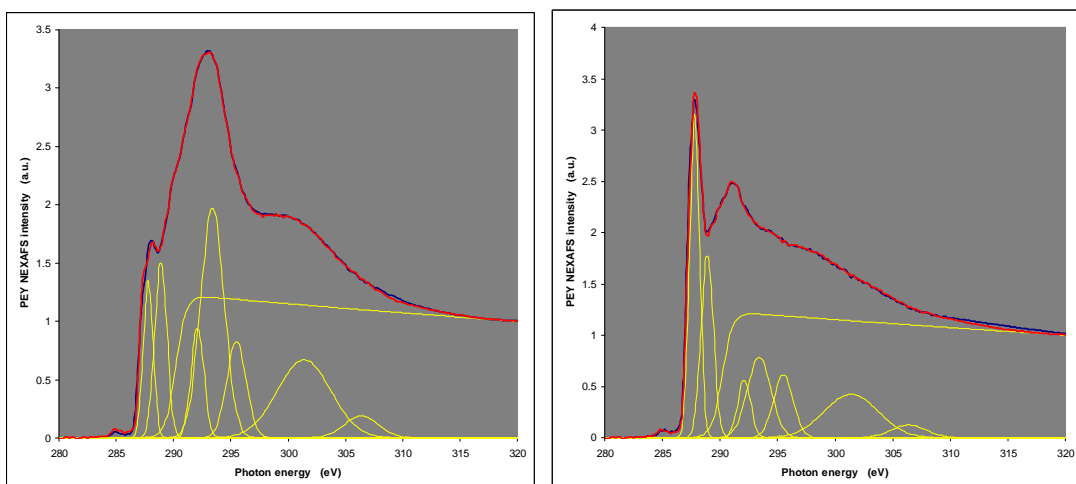


Figure 4. The fitted data for the 10mTorr sample of the pressure series with octadecylphosphonic acid on ITO/Si. On the left is the “grazing” angle 20° and on the right the “normal” angle 90° .

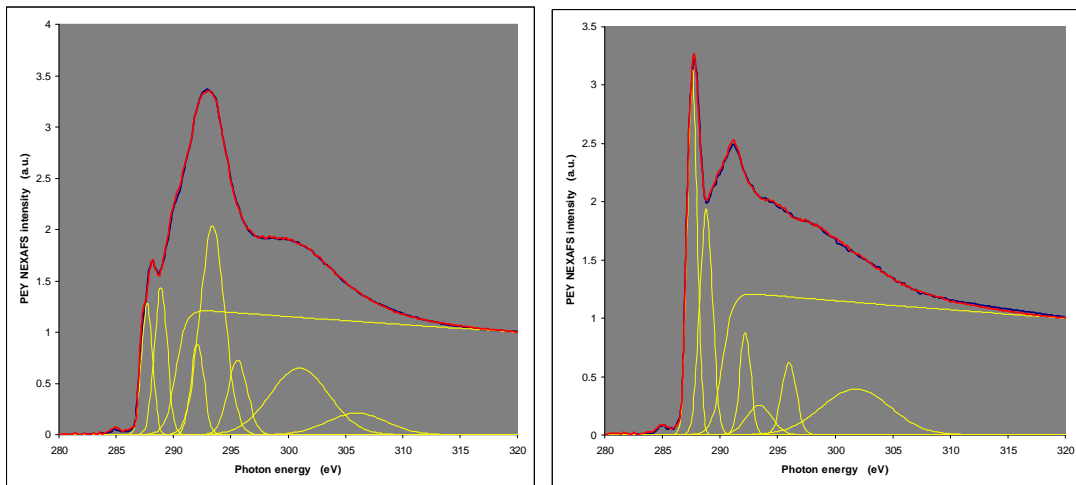


Figure 5. The fitted data for the 12mTorr sample of the pressure series with octadecylphosphonic acid on ITO/Si. On the left is the “grazing” angle 20° and on the right the “normal” angle 90°

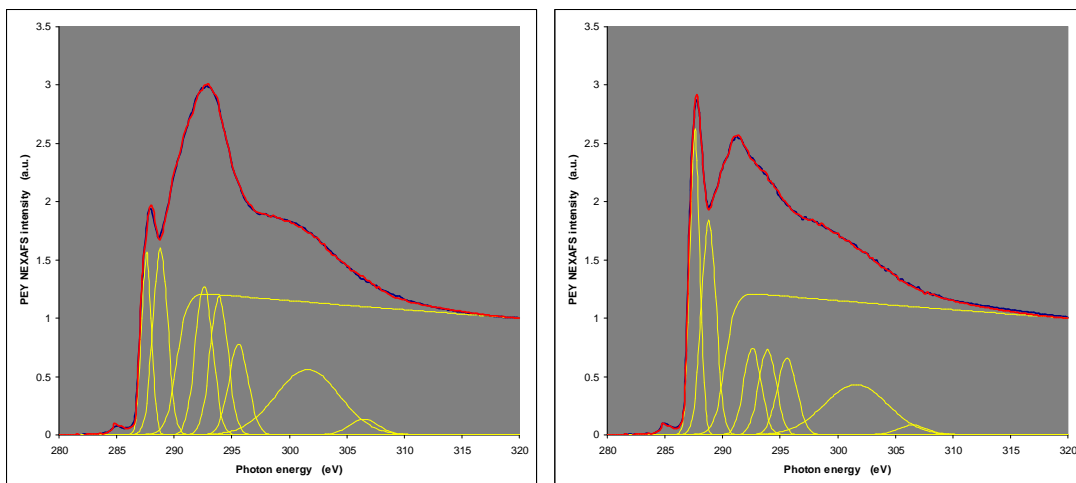


Figure 6. The fitted data for the 15mTorr sample of the pressure series with octadecylphosphonic acid on ITO/Si. On the left is the “grazing” angle 20° and on the right the “normal” angle 90°

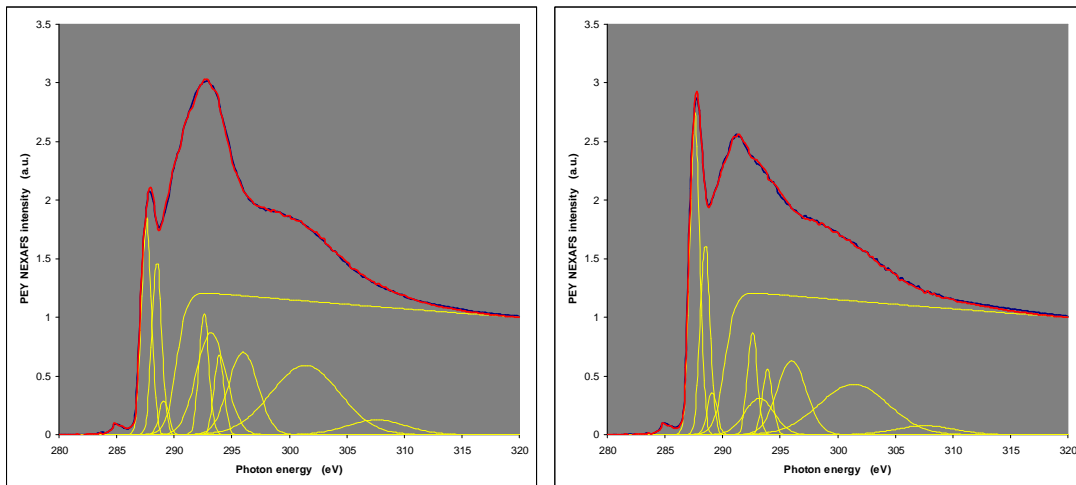


Figure 7. The fitted data for the 20mTorr sample of the pressure series with octadecylphosphonic acid on ITO/Si. On the left is the “grazing” angle 20° and on the right the “normal” angle 90°

The following graphs represent the calculated tilt angles for the rest of the pressure series on the octadecylphosphonic acid corresponding to the 6mTorr sample in the text. Each graphs represents the what the approximate angles for each sample are as shown in table 1.

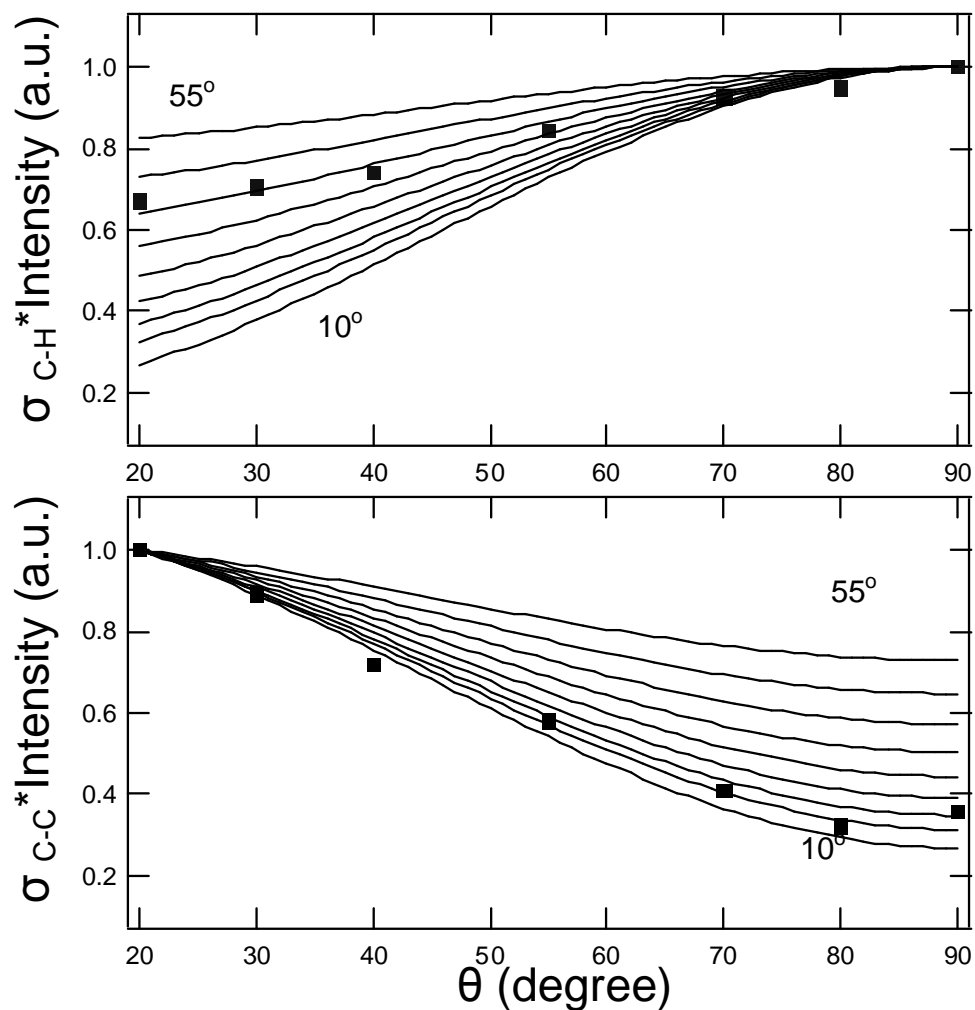


Figure 8. The peak areas for the 4mTorr sample with octadecylphosphonic acid on ITO/Si. The top graph shows the peak area for the $1s \rightarrow \sigma_{C-H^*}$ and the bottom graph show the peak are for the $1s \rightarrow \sigma_{C-C^*}$. Each of the lines represents different chain tilt angles (starting at 10° , shown on graph, 20, 25, 30, 35, 40, 45, 50, 55, shown on graph) evaluated using Reference 7.

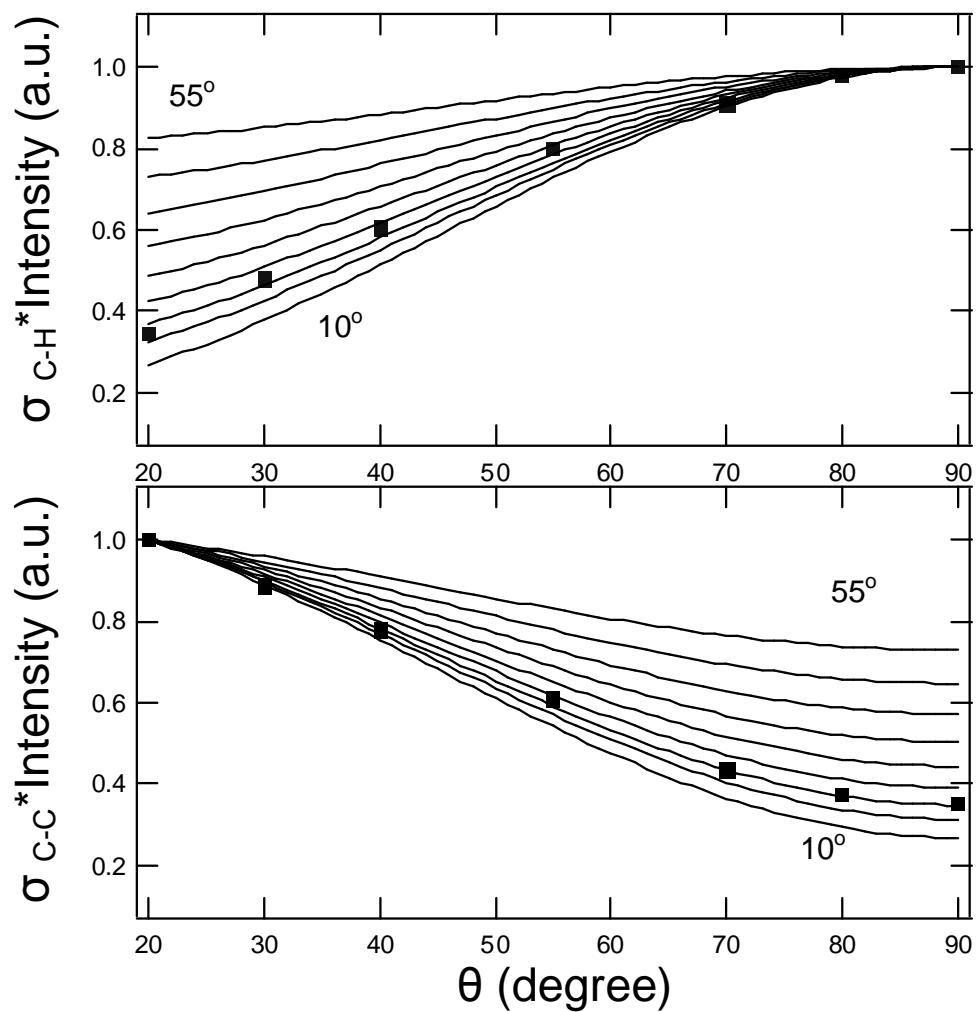


Figure 9. The peak areas for the 8mTorr sample with octadecylphosphonic acid on ITO/Si. The top graph shows the peak area for the $1s \rightarrow \sigma_{C-H^*}$ and the bottom graph show the peak are for the $1s \rightarrow \sigma_{C-C^*}$. Each of the lines represents different chain tilt angles (starting at 10° , shown on graph, 20, 25, 30, 35, 40, 45, 50, 55, shown on graph) evaluated using Reference 7.

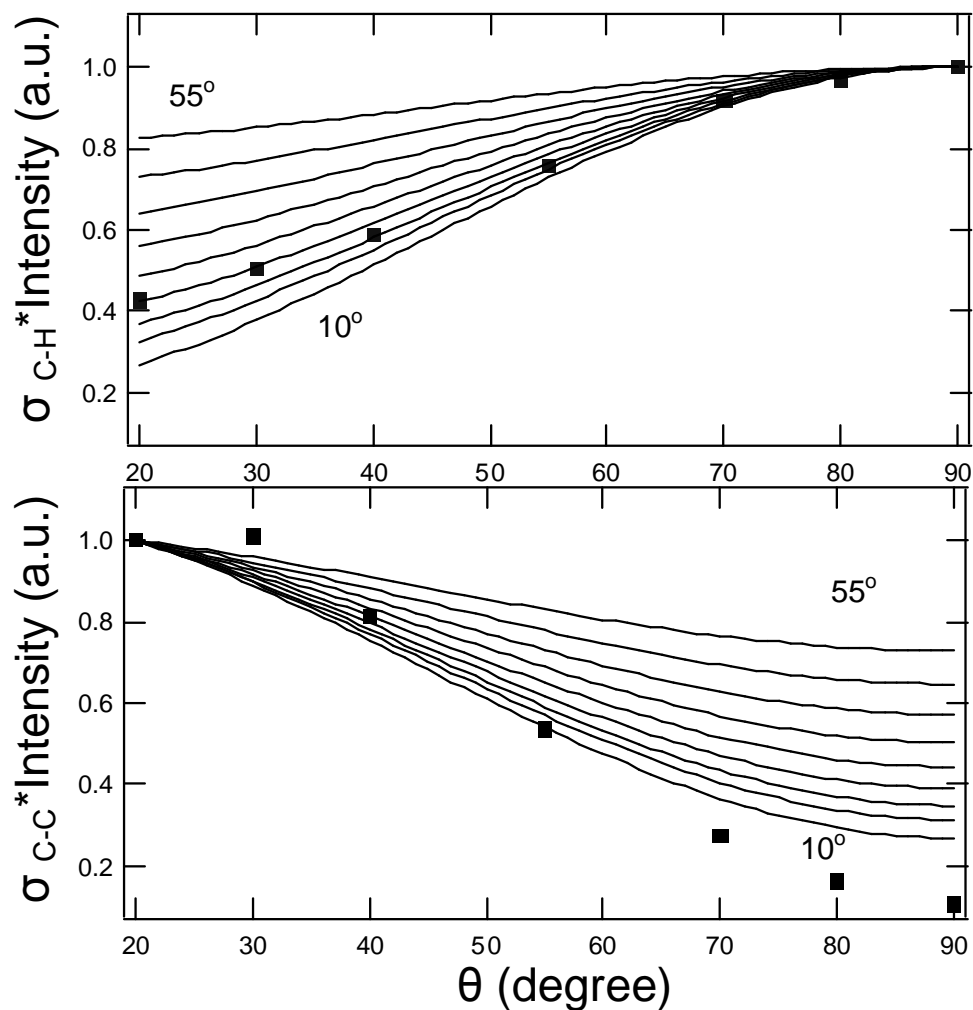


Figure 10. The peak areas for the 9mTorr sample with octadecylphosphonic acid on ITO/Si. The top graph shows the peak area for the $1s \rightarrow \sigma_{C-H^*}$ and the bottom graph show the peak are for the $1s \rightarrow \sigma_{C-C^*}$. Each of the lines represents different chain tilt angles (starting at 10° , shown on graph, 20, 25, 30, 35, 40, 45, 50, 55, shown on graph) evaluated using Reference 7.

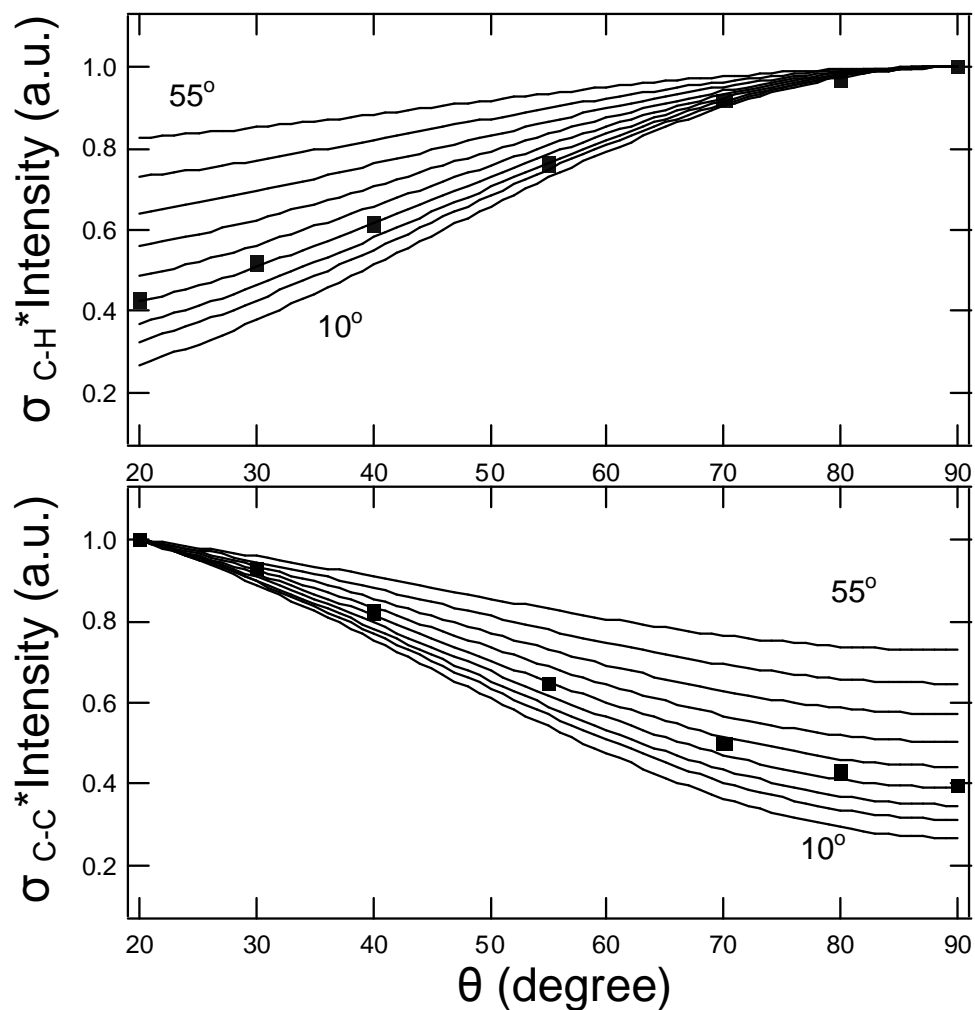


Figure 11. The peak areas for the 10mTorr sample with octadecylphosphonic acid on ITO/Si. The top graph shows the peak area for the $1s \rightarrow \sigma_{C-H}^*$ and the bottom graph show the peak are for the $1s \rightarrow \sigma_{C-C}^*$. Each of the lines represents different chain tilt angles (starting at 10° , shown on graph, 20, 25, 30, 35, 40, 45, 50, 55, shown on graph) evaluated using Reference 7.

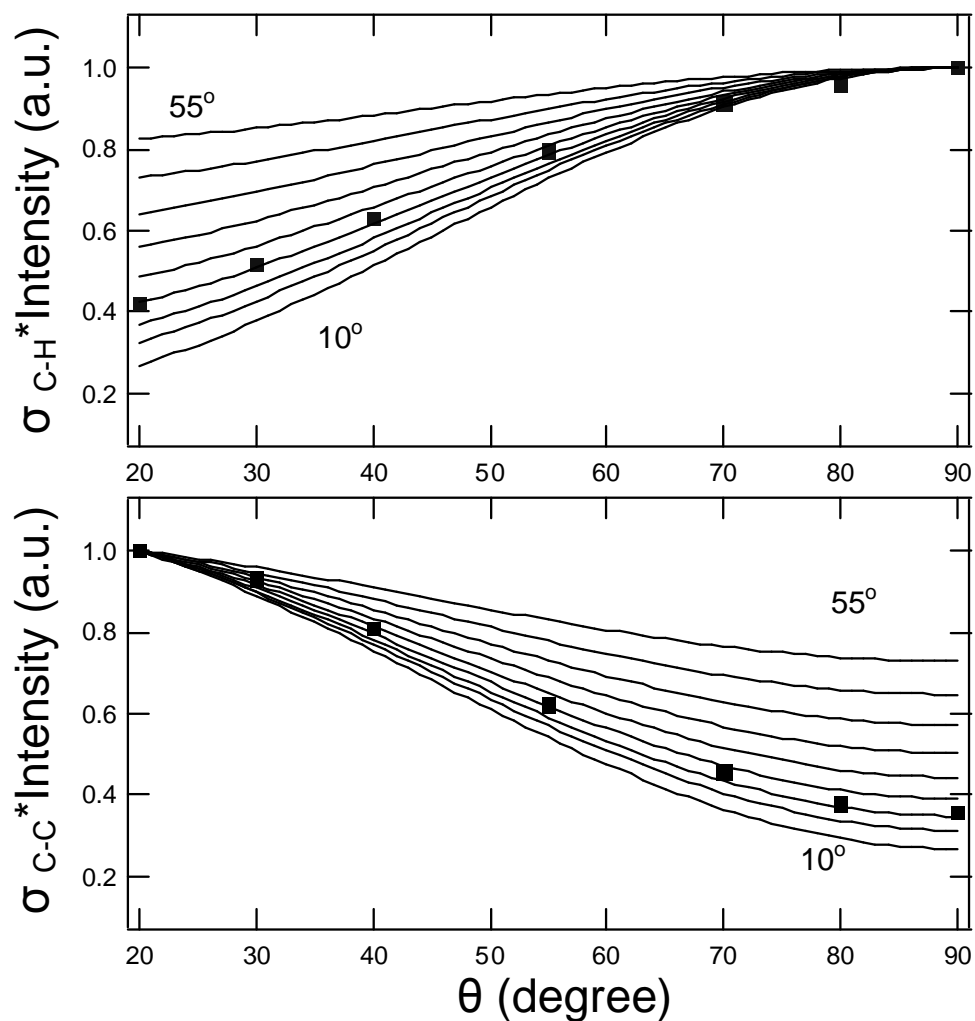


Figure 12. The peak areas for the 12mTorr sample with octadecylphosphonic acid on ITO/Si. The top graph shows the peak area for the $1s \rightarrow \sigma_{C-H^*}$ and the bottom graph show the peak are for the $1s \rightarrow \sigma_{C-C^*}$. Each of the lines represents different chain tilt angles (starting at 10° , shown on graph, 20, 25, 30, 35, 40, 45, 50, 55, shown on graph) evaluated using Reference 7.

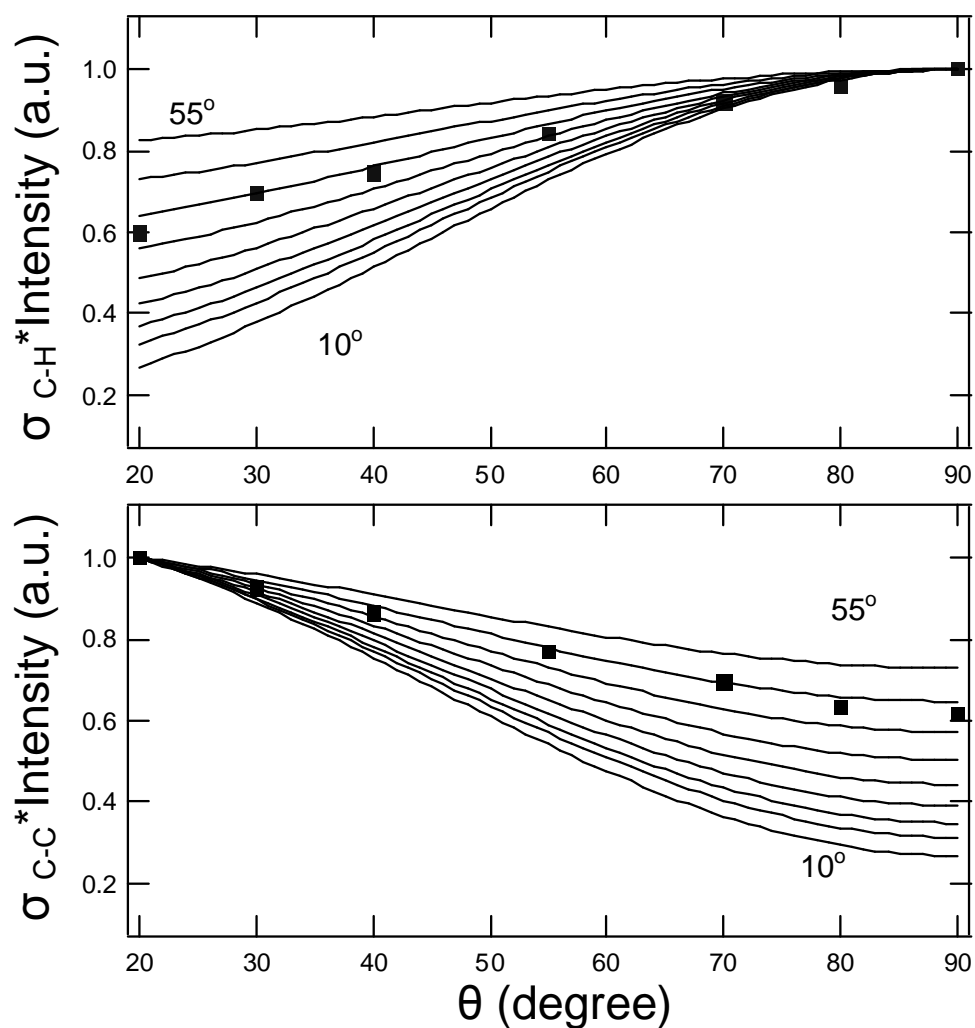


Figure 13. The peak areas for the 15mTorr sample with octadecylphosphonic acid on ITO/Si. The top graph shows the peak area for the $1s \rightarrow \sigma_{C-H^*}$ and the bottom graph show the peak are for the $1s \rightarrow \sigma_{C-C^*}$. Each of the lines represents different chain tilt angles (starting at 10° , shown on graph, 20, 25, 30, 35, 40, 45, 50, 55, shown on graph) evaluated using Reference 7.

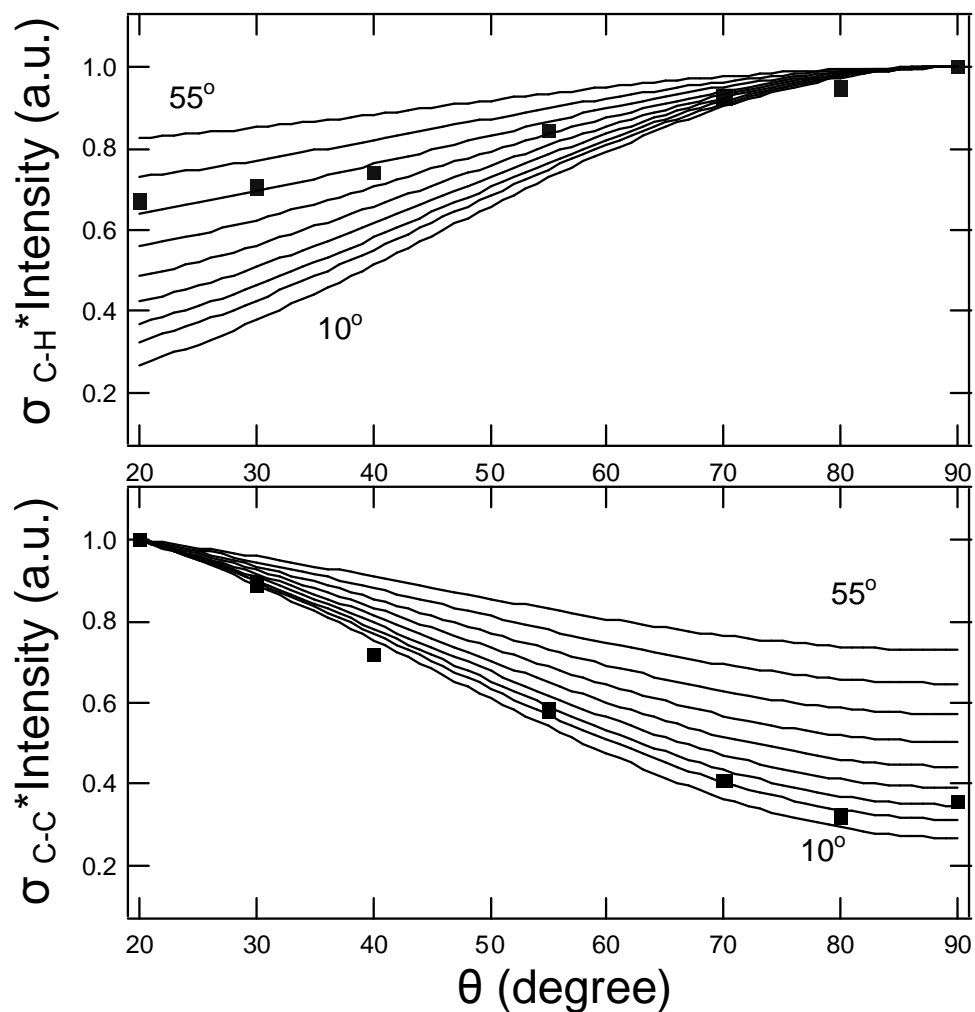


Figure 14. The peak areas for the 20mTorr sample with octadecylphosphonic acid on ITO/Si. The top graph shows the peak area for the $1s \rightarrow \sigma_{C-H}^*$ and the bottom graph show the peak are for the $1s \rightarrow \sigma_{C-C}^*$. Each of the lines represents different chain tilt angles (starting at 10° , shown on graph, 20, 25, 30, 35, 40, 45, 50, 55, shown on graph) evaluated using Reference 7.